Hydrate dissolution as a potential mechanism for pockmark formation in the Niger delta

N. Sultan,[1] B. Marsset,[1] S. Ker,[1] T. Marsset,[1] M. Voisset,[1] A. M. Vernant,[1,2] G. Bayon,[1] E. Cauquil,[3] J. Adamy,[3] J. L. Colliat,[3] and D. Drapeau[3]

Received 17 February 2010; accepted 9 March 2010; published 11 August 2010.

[1] Based on acquired geophysical, geological and geotechnical data and modeling, we suggest hydrate dissolution to cause sediment collapse and pockmark formation in the Niger delta. Very high-resolution bathymetry data acquired from the Niger delta reveal the morphology of pockmarks with different shapes and sizes going from a small ring depression surrounding an irregular floor to more typical pockmarks with uniform depression. Geophysical data, in situ piezocone measurements, piezometer measurements and sediment cores demonstrate the presence of a common internal architecture of the studied pockmarks: inner sediments rich in gas hydrates surrounded by overpressured sediments. The temperature, pressure and salinity conditions of the studied area have allowed us to exclude the process of gas-hydrate dissociation (gas hydrate turns into free gas/water mixture) as a trigger of the observed pockmarks. Based on numerical modeling, we demonstrate that gas-hydrate dissolution (gas hydrate becomes mixture of water and dissolved gas) under a local decrease of the gas concentration at the base of the gas-hydrate occurrence zone (GHOZ) can explain the excess pore pressure and fluid flow surrounding the central hydrated area and the sediment collapse at the border of the GHOZ. The different deformation (or development) stages of the detected pockmarks confirm that a local process such as the amount of gas flow through faults rather than a regional one is at the origin of those depressions.

Citation: Sultan, N., et al. (2010), Hydrate dissolution as a potential mechanism for pockmark formation in the Niger delta, *J. Geophys. Res.*, *115*, B08101, doi:10.1029/2010JB007453.

1. Introduction

[2] Pockmarks have been identified and reported in many areas around the world in various depositional systems, occurring in both random and nonrandom distributions and at different water depths. *Gay et al.* [2006] and *Pilcher and Argent* [2007] have recently described and summarized several mechanisms for developing and maintaining pockmarks as the presence of buried channels [e.g., *Haskell et al.*, 1997], mud diapirs [e.g., *Dimitrov and Woodside*, 2003], and sediment slumps [e.g., *Foland et al.*, 1999]. Pockmarks are also widely recognized to have formed as a result of fluid and gas seepage through the seabed [*Hovland et al.*, 2002; *Hovland et al.*, 2005; *Judd and Hovland*, 2007], are sometimes clearly associated with underlying gas chimneys [*Hustoft et al.*, 2007], but mechanisms through which seepage occurs and the seabed is deformed remain poorly known.

[3] Gas hydrate has been commonly found in sediments at the floor or at shallow depth below the seabed of pockmarks located in the hydrate stability zone of continental slopes [i.e., *Sahling et al.*, 2008], but the role of gas hydrate in the dynamics of formation of pockmarks remain questioned. Pockmarks associated with gas (free or dissolved) and gas hydrates are important globally (1) to assess the methane release from the seabed to the ocean and ultimately to the atmosphere in climatic studies investigating methane as a greenhouse gas [*Badr et al.*, 1991], (2) because methane emissions from pockmarks are a driving force of cold seep ecosystems hosting unique biota [*Foucher et al.*, 2009], and (3) because pockmarks are often found in continental slope areas of fluid-driven sedimentary failure of concern to the deep offshore industry.

[4] The Niger delta is an area where many seep-related seabed features have been found over the last years in particular during industry exploration mapping at water depths between 500 and 1500 m [*Hovland et al.*, 1997; *Brooks et al.*, 2000; *Georges and Cauquil*, 2007]. Various studies from the Nigerian continental slope have shown different seafloor sedimentary features such as pockmarks, gas hydrates, slides, mud volcanoes, and carbonate buildups associated with fluid flow [*Damuth*, 1994; *Cohen and McClay*, 1996; *Brooks et al.*, 2000; *Haskell et al.*, 1999;

[1]Département Géosciences Marines, Ifremer, Plouzané, France.
[2]Now at Cathie Associates, Diegem, Belgium.
[3]Total, France.

0148-0227/10/2010JB007453

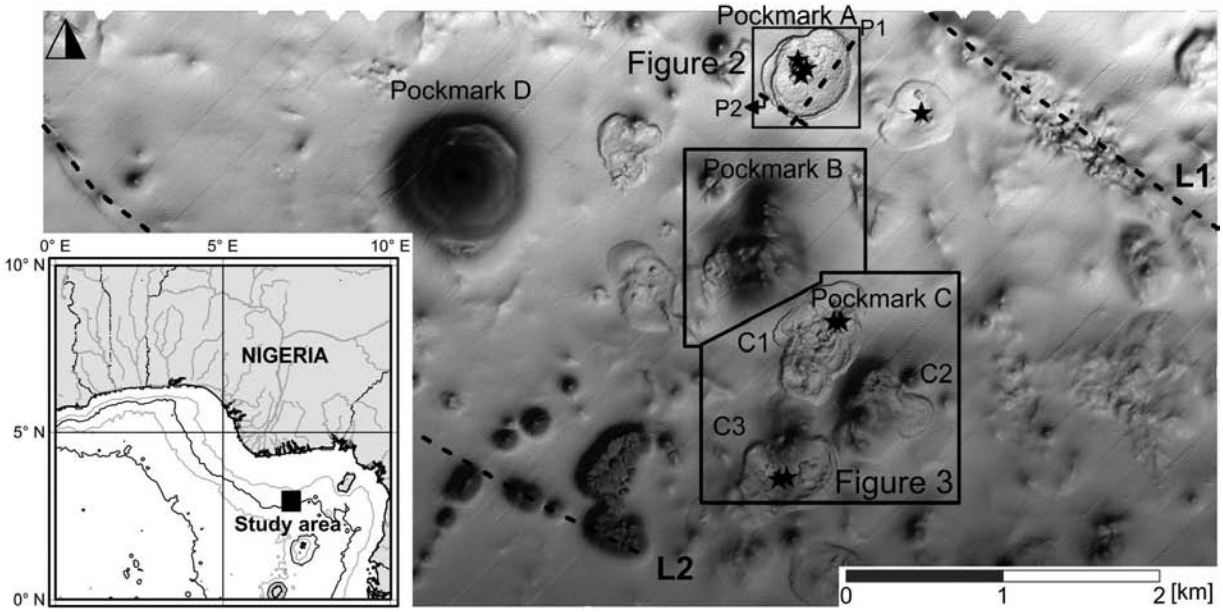

Figure 1. Shaded AUV bathymetric map in region of the Niger delta showing different pockmark shapes and sizes [*Georges and Cauquil*, 2007]. Most of these pockmarks are located within a NW-SE trend area bounded by two lineaments (L1 and L2) corresponding to deep-rooted normal faults. Massive gas hydrates recovered by coring are indicated by stars.

Hovland et al., 1997; *Deptuck et al.*, 2003, among others]. *Heggland* [2003] observed gas chimneys above hydrocarbon-charged reservoirs. These chimneys are believed to result from hydrocarbon dysmigration (leakage of petroleum from a trap) along fault planes between source rocks of reservoirs and the seabed. All these observations make the Niger delta a prime interest target to study the active interplay of fluid flow processes, gas-hydrate dynamics, and seafloor deformation. In this work we focus on a specific area, where very high-resolution bathymetry data (autonomous underwater vehicles, or AUV, data from *Georges and Cauquil*, 2007) acquired recently (Figure 1) show the presence of pockmarks with different shapes and sizes. Some pockmarks are associated to buried channels; others are linked to surface and subsurface faults or to the occurrence of gas hydrates. In this work, we study this last type of pockmark where gas-hydrate dynamics could play an important role in the formation and development of pockmarks. We investigate (using various methods: geophysics, geotechnics, and geology) whether the shape and morphology of theses pockmarks could be controlled by gas-hydrate dynamics. Finally, we use numerical modeling to validate assumptions and working hypothesis about the possible link between pockmarks formation and evolution and gas-hydrate dissolution processes.

2. Geological Setting

[5] The study area is located in the Gulf of Guinea on the west coast of central Africa, south of Nigeria and seaward of the modern Niger delta (Figure 1). The continental margin off the Niger delta is undergoing deformation by gravity-driven tectonism mainly initiated in response to rapid seaward progradation and to sediment loading of the successive depocenters [*Damuth*, 1994]. The Niger delta can be subdivided into five major structural provinces [*Corredor et al.*, 2005]: (1) an extensional province characterized by extensive listric growth faults, (2) a diapiric belt, (3) an inner fold and thrust belt, (4) a transitional detachment fold zone characterized by little or no deformation interspersed with large detachment folds, and (5) an outer fold and thrust belt. The two fold and thrust belts are interpreted as the product of contraction caused by gravity-driven extension on the shelf [*Corredor et al.*, 2005]. These structural provinces indicate that large portions of the thick sedimentary prism are slowly moving downslope by gravity gliding or sliding on decollement level, located within the "mobile shales" series, in a manner analogous to giant mass movements or mega-landslides.

[6] The investigated area which is characterized by numerous circular to subcircular features lies at water depths ranging from ~1100 to 1250 m and is located in the transitional detachment zone of *Corredor et al.* [2005] (Figure 1). Most of these features are located within a NW-SE trending area bounded by two lineaments clearly expressed on the bathymetric map (Figure 1). The two lineaments (L1 and L2 in Figure 1) correspond to deep-rooted normal faults, which delineate a graben collapsed zone linked to the axis of a subsurface anticline structure.

[7] A set of very high-resolution bathymetry (VHR) data, 3-D seismic data [*Georges and Cauquil*, 2007], and deep towed VHR data was acquired recently in the study area. The data reveal a field of pockmarks, each of them several tens to a few hundreds of meters wide, ranging in shape from a slightly depressed, hummocky seafloor (i.e., Figure 1-Figure 3, pockmarks A, B, and C) to a much more pronounced depression (i.e., Figure 1, pockmark D).

[8] The various morphologies of these pockmarks suggest distinct modes of formation, or possibly different stages of evolution. In addition, recovered sediment cores showed

massive gas-hydrate occurrences at several coring sites (sites shown by stars in Figure 1). Based on geophysical data, coring results, and in situ measurements, gas hydrate seems densely accumulated within a few meters thick sediment layers at shallow depth below the floor of the pockmarks [*Sultan et al.*, 2007].

3. Tools and Methods

[9] Geotechnical, geophysical, and geological data used in this work were acquired within the framework of two joint research projects (NERIS with two oceanographic cruises in 2004 and ERIG3D with one oceanographic cruise in 2008) between Ifremer and TOTAL. Parts of the geotechnical and geophysical data acquired during the two NERIS cruises were published by *Sultan et al.* [2007].

3.1. Piston Cores, Laboratory Tests, and Geochemical Analysis

[10] Sediment samples collected from the study area with piston corers during the ERIG3D cruise had penetrations between 3 and 6 m. In order to identify the key mechanical and physical parameters of the sediments, an onboard experimental program on undisturbed marine sediment samples has been undertaken. Log sediment cores using the GEOTEK core logging devices (MSCL) was first carried out using the following sensors:

[11] - Ultrasonic transducers to measure the velocity of compressional waves in the core.

[12] - A gamma ray source and detector for measuring the attenuation of gamma rays through the core (providing density/porosity values).

[13] The detailed onboard laboratory geotechnical investigation also includes classification tests, strength tests, and *P* wave velocity measurements using laboratory celerimeter. The classification tests include unit weight and moisture content determinations. Shear strengths were performed using the vane shear on undisturbed samples.

[14] The compositions and concentrations of gases in the sediment were determined using the headspace method (see for instance *Kvenvolden and Redden* [1980]). Immediately after retrieval of the sediment cores on deck, headspace gas samples were taken from the ends of cut sections and sealed in calibrated steel container.

3.2. Piezocone

[15] In situ geotechnical measurements were carried out using the Ifremer piezocone (called PENFELD). It is equipped with a rod which penetrates the sediment to a maximum depth of 30 m. The 36 mm diameter rod is coiled around a 2.20 m diameter drum and is straightened during penetration using the "coiled tubing" technique. In the Cone Penetration Test (CPTU) a cone on the end of coiled tubing is pushed into the soil layers at a constant rate. The electric cone (10 cm^2) gives a continuous measurement of the tip resistance (qc), sleeve friction (fs), and excess pore pressure (Δu_2) measured by means of a porous filter located immediately behind the cone (called u_2 type cone). The Ifremer CPTU uses a hydrostatically compensated system where the cone load sensor is unaffected by the hydrostatic pressures leading to greater accuracy and sensitivity measurements in soft sediments [*Andersen et al.*, 2008]. The geometry of the cone penetrometer with tip, sleeve, and pore pressure filters follows ISO/DIS 22476-1.

3.3. Piezometer

[16] The Ifremer piezometer was used during the ERIG3D cruise. It is a free-fall device with a sediment-piercing lance attached to a recoverable instrument part [*Sultan et al.*, 2009]. It is ballasted with lead weights to penetrate a range of sediment types in water depths of up to 6000 m. The length of the lance used depends on the stiffness of the sediment with a maximum length of 12 m. Pore pressures are measured relative to hydrostatic pressure at different ports on the 60 mm diameter lance using specially adapted differential pressure transducers connected to the pressure ports and the open seawater. The piezometer pore pressure sensors have an accuracy of ±0.4 kPa. The piezometer lance is also equipped with temperature sensors located at the same level as the pore pressure sensors. Temperature sensors have an accuracy of 0.05°C. A total of two short-term piezometers measurements were carried out (PZY01 and PZY02) at two different locations in pockmark A (Figure 2). The aim was to characterize the hydraulic regime at the periphery of pockmark A and above the suspected gas-hydrate occurrence zone (GHOZ).

3.4. Geophysical Data

[17] Pre-existing geophysical data were made available by Total. A major input was the velocity field derived from an exploration 3-D data set. The shallow part of the seismic data was reprocessed using an automatic 3-D high-density velocity analysis tool [D-stack analysis; *Arnaud et al.*, 2004], allowing the detection of anomalous values related to the presence of gas hydrates and carbonated crusts (Figure 2 and Figure 3). Previous subbottom profiler (SBP) and multibeam data from an AUV site survey were used to characterize the bathymetry and the seafloor morphology at a detailed scale. The SBP data set included a pseudo-3-D survey of the northern pockmark (Pockmark A - for location see Figure 1) displaying remarkable details with a bin size of one meter [*Georges and Cauquil*, 2007].

[18] New geophysical seismic data were acquired during the ERIG3D cruise with the recently developed SYSIF deep towed acquisition system [*Ker et al.*, 2008; *Marsset et al.*, 2010]. SYSIF is a heavy towed apparatus hosting low-frequency acoustic transducers (250–1000 Hz, 650–2000 Hz) and a single-channel streamer in order to provide high-resolution (HR) images of the subbottom. The altitude of SYSIF over the seafloor is set to 100 m thus reducing the Fresnel zone (i.e., enhancing the lateral resolution compared to conventional surface towed systems). More details about SYSIF system are given by *Ker et al.* [2008] and *Marsset et al.* [2010].

3.5. Gas-Hydrate Modeling

3.5.1. Gas Hydrate: Stability Law and Excess Pore Pressure Generated by Hydrate Dissolution/Dissociation

[19] In recent years, numerous theoretical models were proposed for the gas-hydrate stability law [*Handa*, 1990; *Rempel and Buffett*, 1997; *Zatsepina and Buffett*, 1997, 1998; *Sloan*, 1998; *Xu and Ruppel*, 1999; *Henry et al.*, 1999; *Clennell et al.*, 1999; *Davie and Buffett*, 2001; *Klauda and Sandler*, 2003; *Sultan et al.*, 2004; *Zhang et al.*,

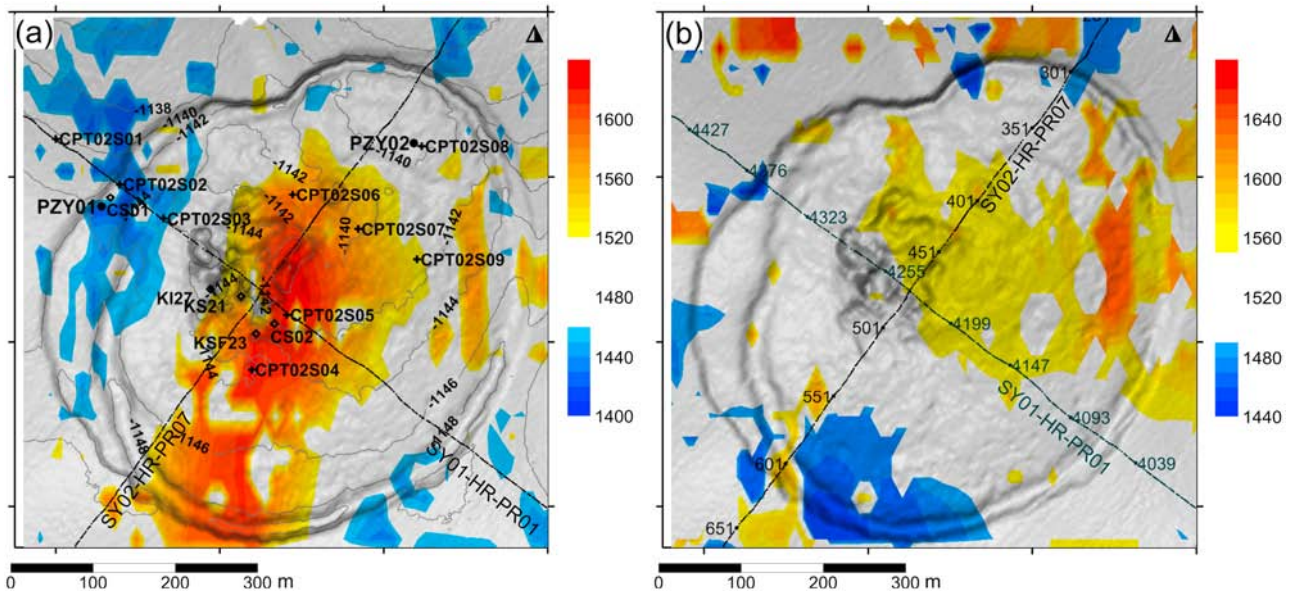

Figure 2. Pockmark A: Interval velocity (color scale in meters per second) obtained from D-stack processing (a) from the upper 15 m and (b) between 15 and 30 m below the seafloor projected on AUV bathymetric maps. Locations of piston cores, piezometers, piezocone measurements and SYSIF profiles (with shot points SP in Figure 2b) are also plotted.

2005]. Most of them are basically derived from the van der Waals's thermodynamic theory [*Van der Waals and Platteeuw*, 1959] with relevant calculated or experimental parameters. In this work, we used two-dimensional gas-hydrate software developed by *Sultan et al.* [2004]. In this software, the temperature and pressure of hydrate-phase equilibrium is calculated by using the Van der Waals's thermodynamic theory and considering the effect of the pore

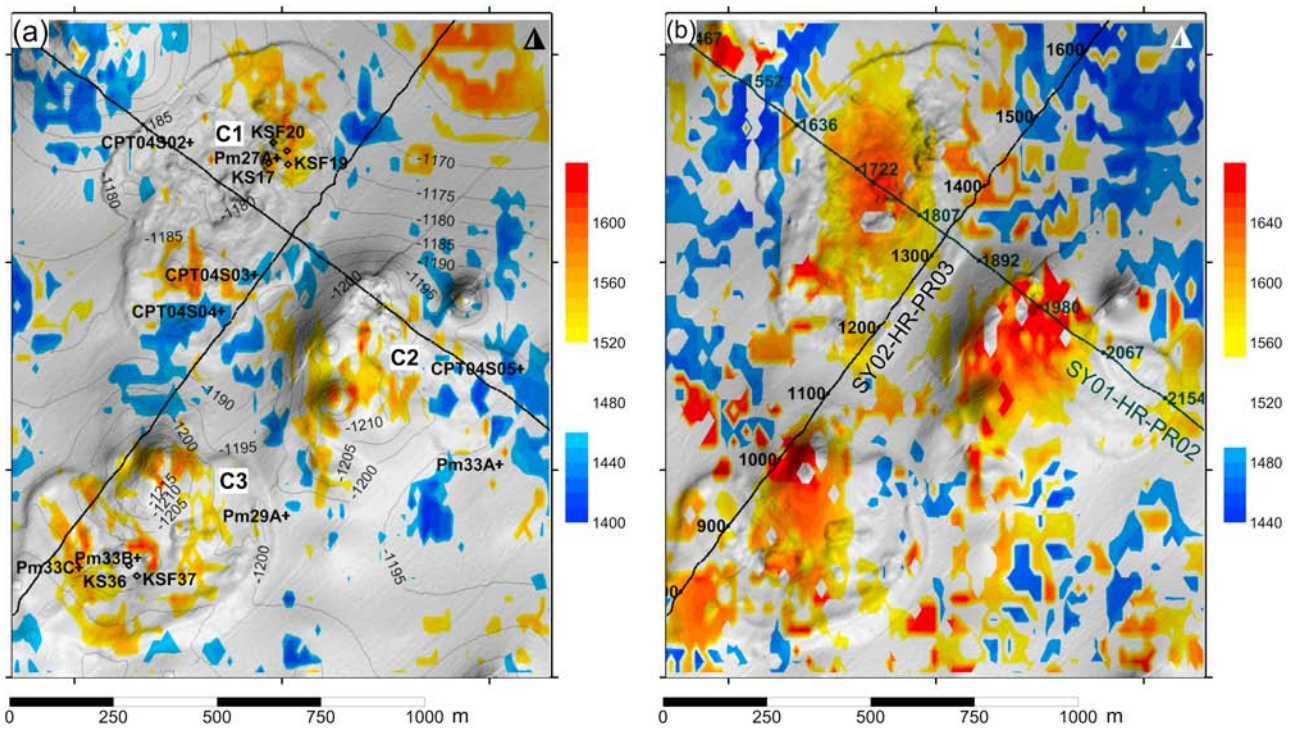

Figure 3. Pockmark C: Interval velocity (color scale in meters per second) obtained from D-stack processing (a) from the upper 15 m and (b) between 15 and 30 m below the seafloor projected on AUV bathymetric maps. Locations of piston cores, piezocone measurements,and SYSIF profiles (with shot points SP in Figure 3b) are also plotted. Pockmark C is composed of three different parts (C1, C2, and C3).

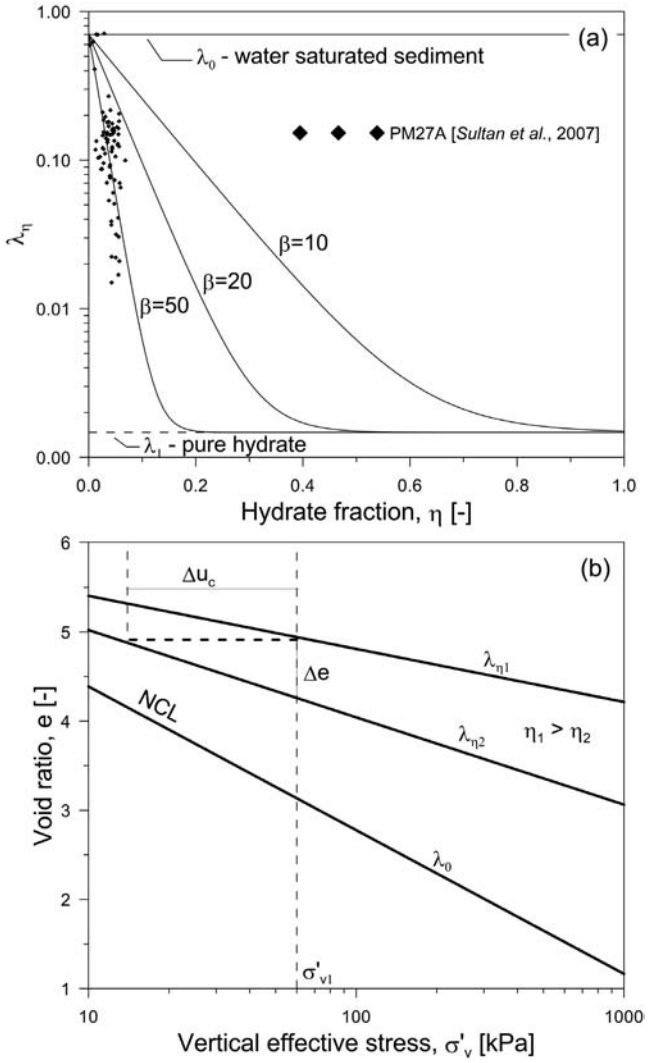

Figure 4. (a) Compression indices of the hydrate-sediment system as a function of the hydrate fraction for three different values of β. Dots correspond to compression indices obtained from in situ piezocone data PM27A [*Sultan et al.*, 2007]. (b) Scheme of the partial decomposition of the gas hydrate and the consequence in terms of excess pore pressure Δu_c (at short term) and sediment compaction Δe (at long term).

water activity and the mean pore size. Heat transfer calculation is done using the conservation of energy equation with the use of a geometric mean model for the thermal conductivity of the medium [*Henninges et al.*, 2005] and a parallel mean model for the volumetric heat capacity. The gas migration is taken into account in terms of dissolved gas diffusion in fluid phase by using Fick's second law supposing that hydrate formation from gas dissolved in liquid water is possible as demonstrated by *Tohidi et al.* [2004] and *Ohmura et al.* [2004]. More recently, *Bigalke et al.* [2009] have shown that hydrate dissolution in undersaturated seawater is a diffusion-controlled process. The methane diffusion coefficient used in the Fick's second law was taken equal to 10^{-9} m^2/s [*Liu and Flemings*, 2006; *Bigalke et al.*, 2009].

[20] The evaluation of the excess pore pressure generated by hydrate dissolution and dissociation and the subsequent dissipation of the pore pressure is carried out by evaluating the excess pore pressure under undrained conditions according to *Sultan* [2007] and *Kwon et al.* [2008]. Additionally, the phenomenon of hydrate dissolution in the gas-hydrate occurrence zone (GHOZ) is considered in this work similar to the destructuration and softening of natural clay where (1) the hydrate formation impedes the normal consolidation of the sediment along the normally consolidated line (NCL) due to the rigidity and stiffness of the cementing agent and (2) the dissolution of the gas hydrate in the GHOZ leads to the compaction (collapse) of the sediment in order to reach the related compressibility line [*Lee et al.*, 2010] which is characterized by a compression index λ_η [*Sultan et al.*, 2007]. The determination of the gas-hydrate-bearing sediment compressibility is based on the following indication: the compression index of the gas-hydrate bearing decreases from the slope of the NCL for purely water saturated soil and tends asymptotically to the pure hydrate compressibility which was identified by *Durham et al.* [2003] to be equal to 0.00147. In this work, the change of the compression index of the hydrate-bearing sediment with the hydrate fraction η is considered through the following equation:

$$\lambda_\eta = \lambda_0[1 - \alpha(1 - \exp(-\beta.\eta))], \tag{1}$$

where λ_0 is the water-saturated sediment compressibility, β defines the slope of the change of the compressibility with the hydrate fraction (Figure 4a) and depends strongly on the distribution of the hydrate within the porous media (cementing or disseminate in the pore). α is calculated from the compressibility of the hydrate phase λ_1 and the water saturated soil compressibility λ_0 according to the following equation:

$$\alpha \approx 1 - \frac{\lambda_1}{\lambda_0}. \tag{2}$$

For the study area, the compression index of the saturated sediment is taken equal to 0.7 [*Sultan et al.*, 2007]. The compression index of the gas-hydrate-bearing sediments was derived from in situ piezocone testing using the *Mitchell and Gardner*'s [1975] empirical equation where the compression index is directly related to the cone resistance *qc*. Based on in situ piezone measurements [site PM27-A; *Sultan et al.*, 2007], the β value for the study area was taken equal to 50 (Figure 4a).

[21] The partial decomposition of the gas hydrate and the change of the compression index $\lambda_{\eta 1}$ to a compression index $\lambda_{\eta 2}$ lead to an excess pore pressure at short-term and sediment compaction at long-term equivalent to the Δe presented in Figure 4b. The determination of the initial excess pore pressure generated by the hydrate decomposition Δu_c is calculated from the following equation:

$$\Delta u_c = \sigma'_{v1} \cdot \left[1 - \frac{1}{\exp\left(\frac{\Delta e}{\lambda_{\eta 2}}\right)}\right], \tag{3}$$

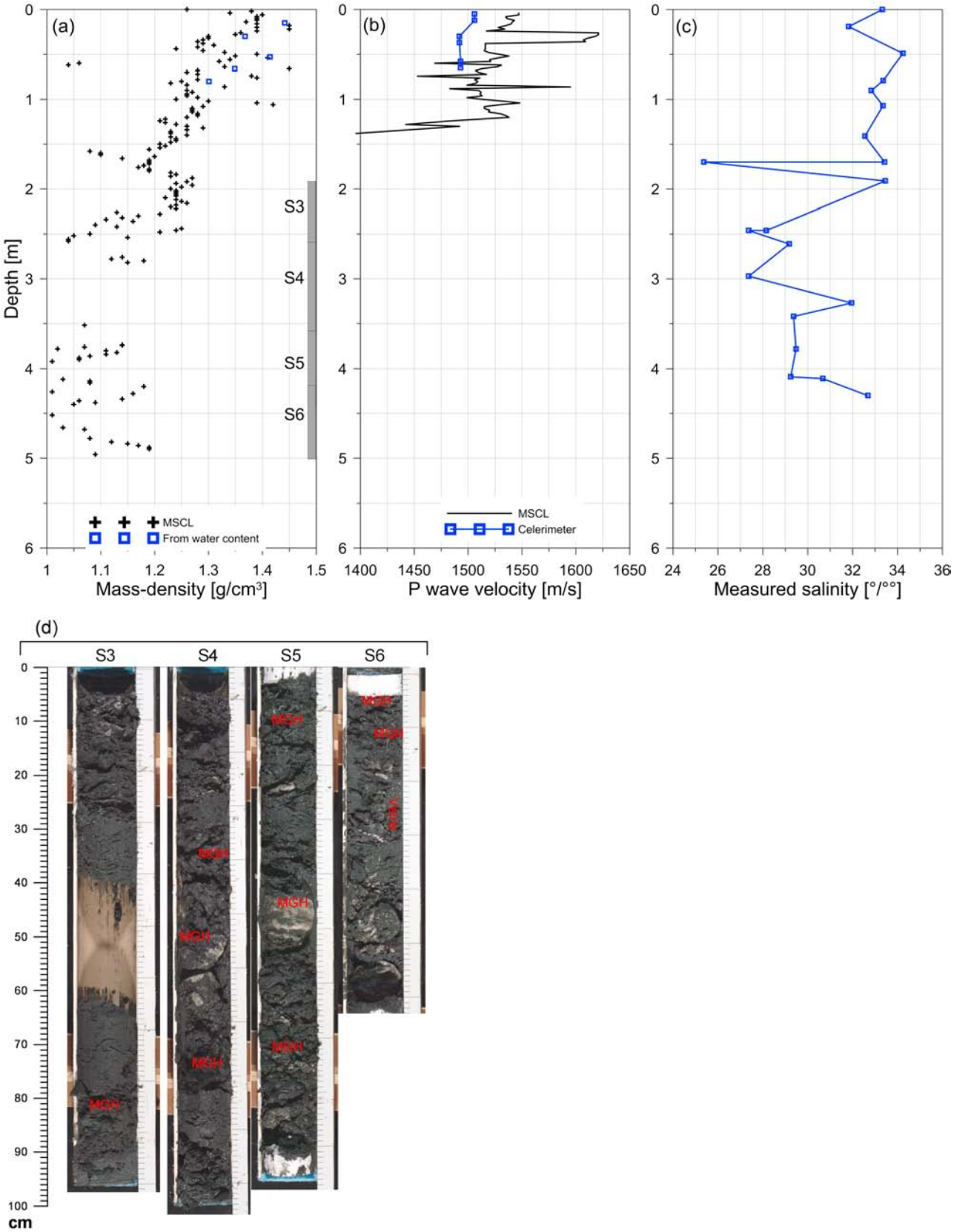

Figure 5. Core CS02: (a) Mass-density, (b) *P* wave velocity, and (c) salinity versus depth [from *Caprais and Pignet*, 2009]. *P* wave velocities are measured using the MSCL logging device and a laboratory celerimeter. (d) Photo images from sections 3 (S3), 4 (S4), 5 (S5), and 6 (S6) showing the presence of high gas-hydrates fractions. (MGH for massive gas hydrates.)

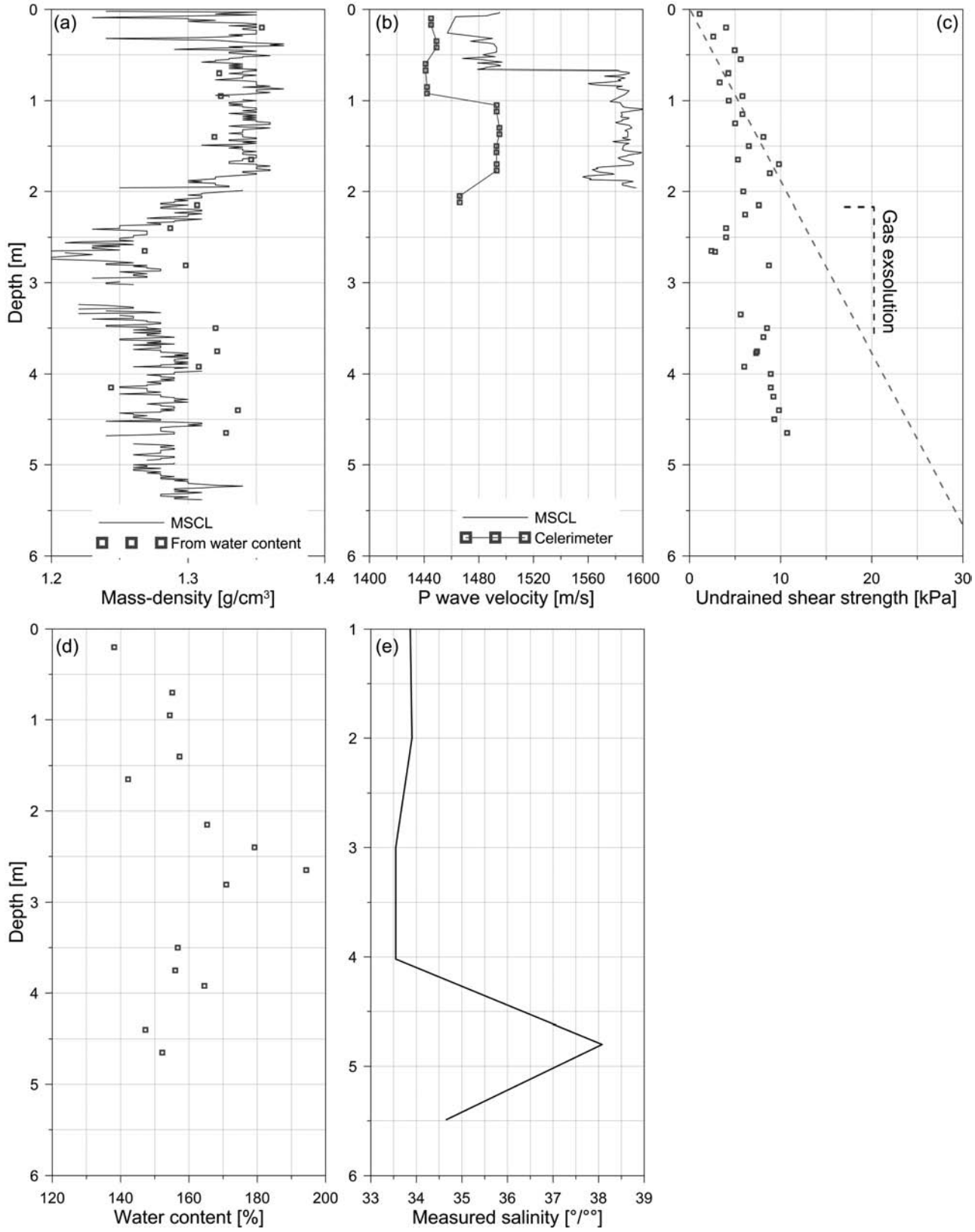

Figure 6. Core CS01: (a) Mass-density, (b) *P* wave velocity, (c) undrained shear strength, (d) water content, and (e) salinity versus depth [from *Caprais and Pignet*, 2009]. *P* wave velocities are measured using the MSCL logging device and a laboratory celerimeter.

Table 1. Compositions and Concentrations of Gases in the Sediment Determined Using the Gas Collection Headspace Method[a]

Core	Section	Hydrate	Molar fraction	
			Methane	Ethane
KSF19		Yes	1	—
KSF20	S1	Yes	0.9989	0.0011
	S2	Yes	1	—
	S3	Yes	1	—
KS21		Yes	1	—
KS30	S2	No	1	—
KSF31	S2	No	1	—
	S2B	No	1	—
	S4B	No	1	—
KSF37	S2B	No	0.9955	0.0045
	S5B	Yes	1	

[a]Only methane and ethane were present for the 6 considered cores.

where Δe is calculated from $\lambda_{\eta 1}$ and $\lambda_{\eta 2}$ and σ'_{v1} corresponds to the vertical effective stress before any sediment compaction (Figure 4b).

[23] The evolution of the pore pressure with time is determined using the Darcy's law equation. The use of the Darcy's law requires the determination of the hydraulic diffusivity of the system which depends on the porosity but also on the gas-hydrate fraction and on how hydrates occupy the pore spaces (see for instance *Waite et al.* [2010]). Several theoretical models were developed in order to define the link between hydrate fraction and relative permeability [*Masuda et al.*, 1997; *Moridis and Pruess*, 1998; *Kleinberg et al.*, 2003, among others]. *Kleinberg et al.* [2003] have proposed two simplified expressions for the relative permeability of water in hydrate-bearing sediment: for hydrate filling the center of the pores and for hydrate covering the grain surface. Recently, *Kumar et al.* [2010] have shown based on experimental results that for initial water saturations greater than 35%, hydrate forms in the pore body, which results in more rapid decline in permeability with increasing hydrate saturation. In this work and in order to calculate the effect of the hydrate fraction on the relative permeability to water we used *Kleinberg et al.*'s [2003] equation where the hydrate is considered filling the center of the pores. At each time step calculation and for each node, the hydraulic diffusivity D_H (which is calculated from the permeability coefficient) is updated as a function of the porosity and the gas-hydrate concentration.

[24] It is important to mention that the excess pore pressure generated by the hydrate dissolution alone without sediment compaction is expected to be very low [*Sultan*, 2007; *Xu and Germanovich*, 2007].

3.5.2. Hydro-fracturing

[25] Fracture developments in low-permeability sediments may be caused by pore pressure (hydraulic fracturing) or free gas pressure (pneumatic fracturing). Several theories applying mechanics of failure to soils were developed during those last two decades in order to evaluate the critical pore pressure that may generate hydraulic fracturing (see for instance *Alfaro and Wong* [2001]). Hydro-fracturing is supposed to occur in sediment whenever the excess pore pressure exceeds the effective least principal stress plus the tensile strength of the medium (see for instance *Alfaro and Wong* [2001]). In a purely lithostatic situation, where sediment is subject to no forces except those of gravity, the greatest effective stress should be vertical (σ'_v) and the least effective stress should be horizontal (σ'_h) [*Sibson*, 2003]. Thus, σ'_h can be calculated from the lateral earth pressure coefficient at rest *Ko* through the following equation:

$$\sigma'_h = Ko.\sigma'_v \tag{4}$$

From the in situ measured sleeve friction and using the relationship proposed by *Masood and Mitchell* [1993], *Ko* is calculated to be between 0.55 and 0.65. The indirect tensile strength of saturated sediment is usually estimated to be one-eight to one-twelfth of unconfined compressive strength [*Schroeder*, 1972]. Based on geotechnical properties acquired from the study area, the tensile strength was considered in this work equal to 10% of the vertical effective stress. Therefore, hydraulic fracturing in saturated clay is considered to occur at 75% of the vertical effective stress.

[26] For gas-hydrate-bearing sediments, the shear strength depends strongly on the hydrate concentration [*Winters et al.*, 2004; *Yun et al.*, 2007; *Masui et al.*, 2008] and may raise significantly its tensile strength value. In the used software and due to the lack of experimental data on shear strength of gas-hydrate-bearing sediment, hydraulic fracturing is considered to occur at 75% of the vertical effective stress for gas-hydrate fraction lower than 5% which corresponds to the limit where gas hydrates seem to have the role of cementing agent in the gas-hydrates-bearing sediments [*Sultan*, 2007]. Moreover, when hydraulic fracturing occurs, fluids must be able to flow from the pressured sediments into the surrounding sediments. That is why a high porosity value (0.95) is assumed in hydraulic fracturing materials with gas-hydrate concentration lower than 5% inducing a significant increase of the hydraulic diffusivity and a decrease of the thermal diffusivity.

4. Results

4.1. From Coring and Geochemical Data

[27] Eight gravity cores (KSF19, KSF20, KS21, KSF23, KS36, KSF37, CS02, and CS03) recovered from the study area showed the presence of massive gas hydrates at different depths below the seafloor (red stars in Figure 1 and locations in Figure 2 and Figure 3).

[28] Figure 5 shows one of those cores (CS02; for location see Figure 2) with the mass-density and *P* wave velocity versus depth measured using the MSCL logging device and the laboratory celerimeter. Figure 5a and 5b show an important decrease of the mass-density and the lost of the *P* wave signal below 1.4 m due to the presence of gas hydrates and free gas. Figure 5c presents photo images from sections 3 (S3), 4 (S4), 5 (S5), and 6 (S6) showing the presence of massive gas hydrates below the bottom of section 3 (Figure 5c). It is also interesting to mention the presence of possible flow conduits in S6 with gas-hydrate-filled veins that could be traced between 25 and 55 cm below the top of the section (Figure 5c). Core CS02 was recovered from an area characterized by high *P* wave velocity anomalies (from 3-D interval velocity analysis; Figure 2).

[29] Core CS01 which was recovered from the periphery of the pockmark A (for location see Figure 2) is presented in

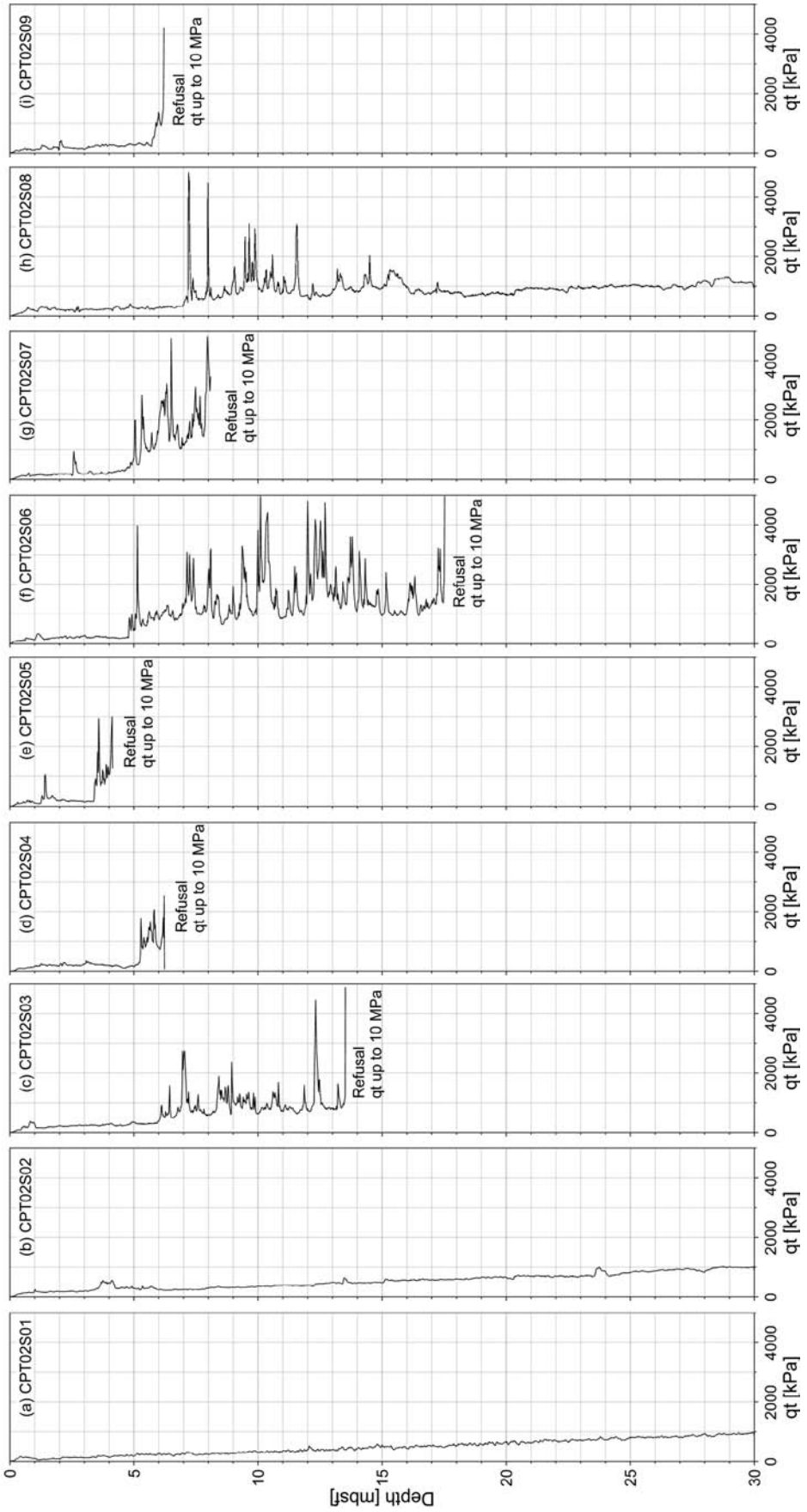

Figure 7. Corrected cone resistance qt versus depth from sites CPT02S01 to CPT02S09.

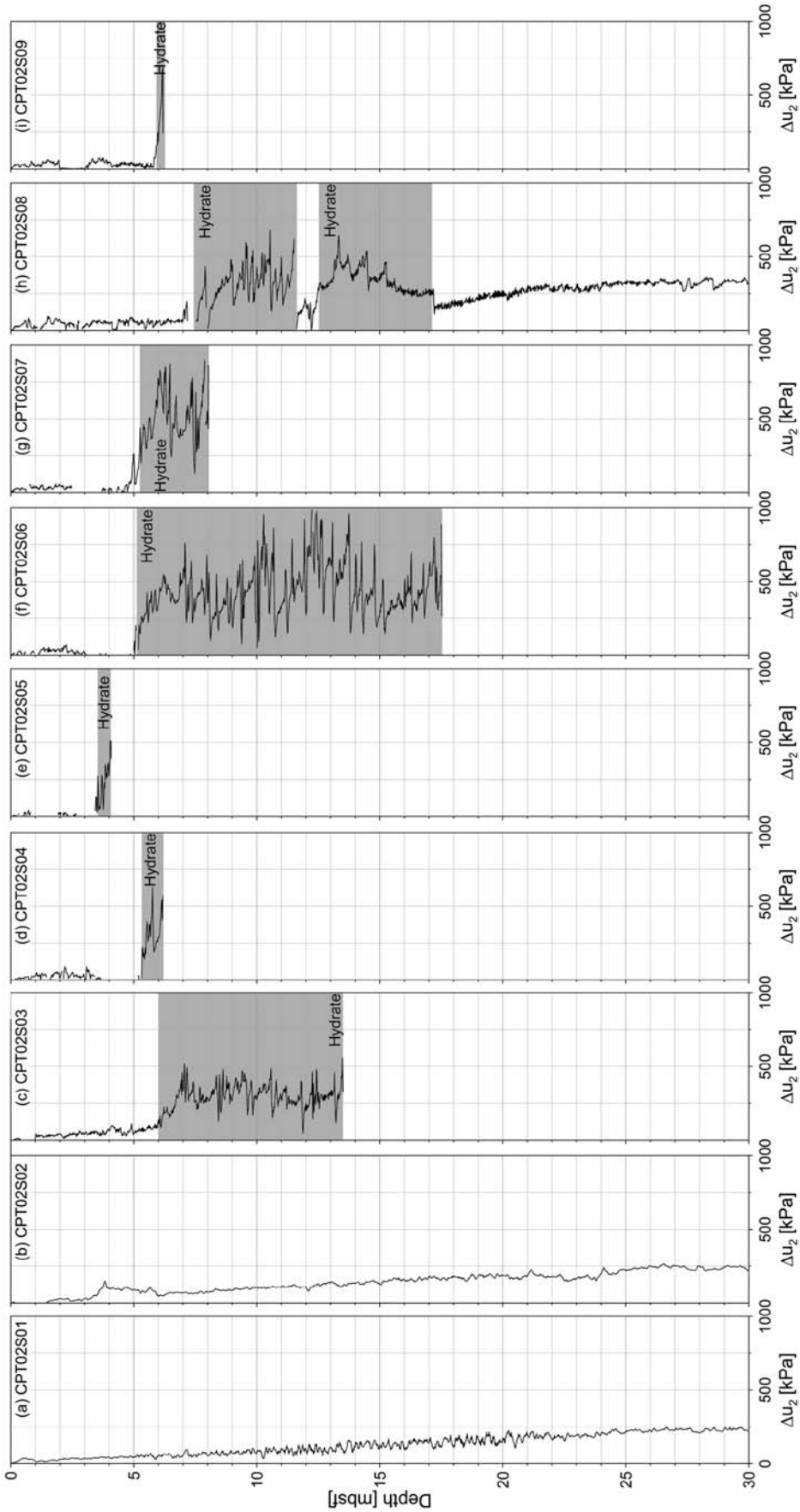

Figure 8. Excess pore pressure Δu_2 versus depth from sites CPT02S01 to CPT02S09. Dashed areas represent suspected gas-hydrates occurrence zones.

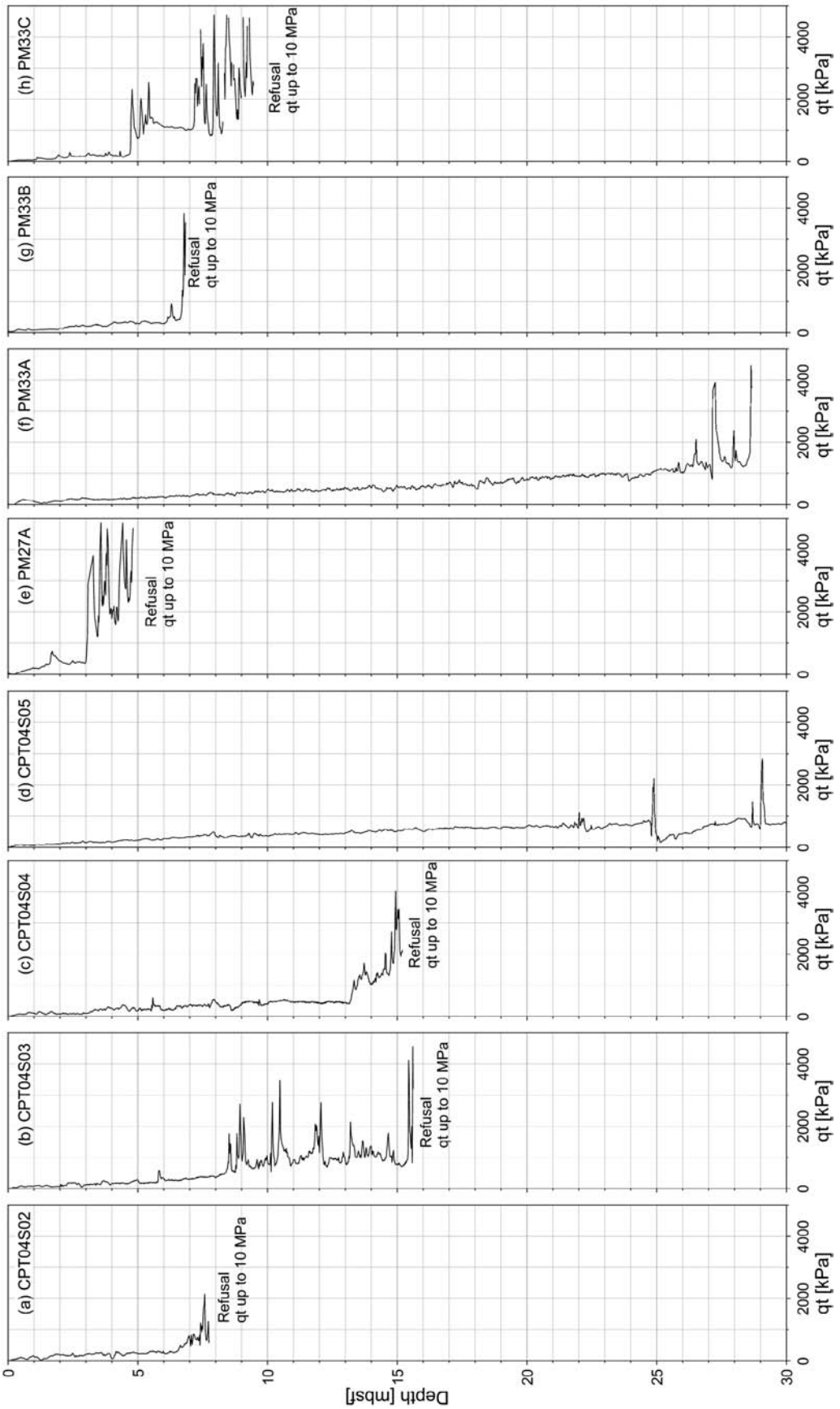

Figure 9. Corrected cone resistance *qt* versus depth from sites CPT04S02, CPT04S03, CPT04S04, CPT04S05, PM27A, PM33A, PM33B and PM33C [data for the last four sites are from *Sultan et al.*, 2007].

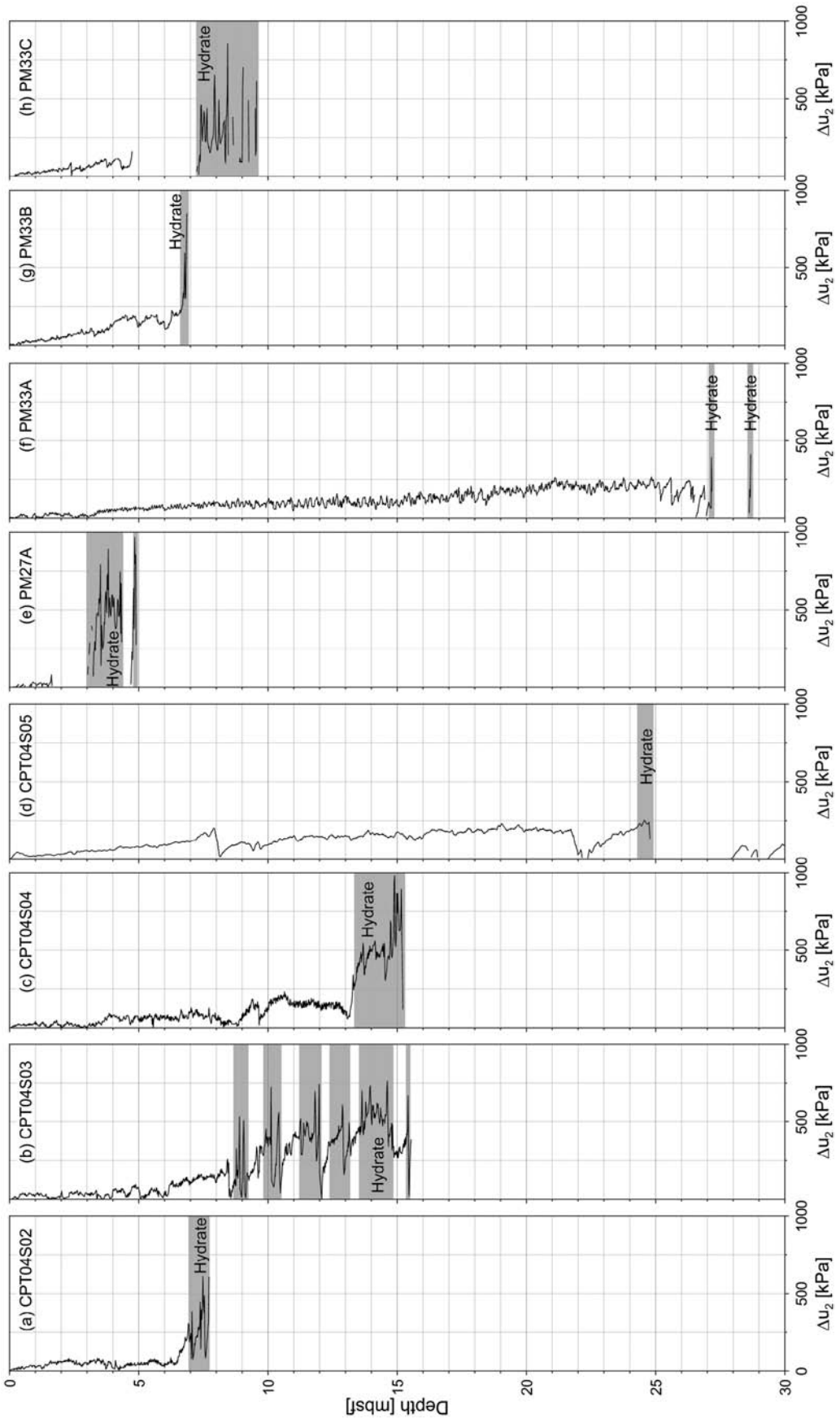

Figure 10. Excess pore pressure Δu_2 versus depth from sites CPT04S02, CPT04S03, CPT04S04, CPT04S05, PM27A, PM33A, PM33B and PM33C [data for the last four sites are from *Sultan et al.*, 2007]. Dashed areas represent suspected gas-hydrates occurrence zones.

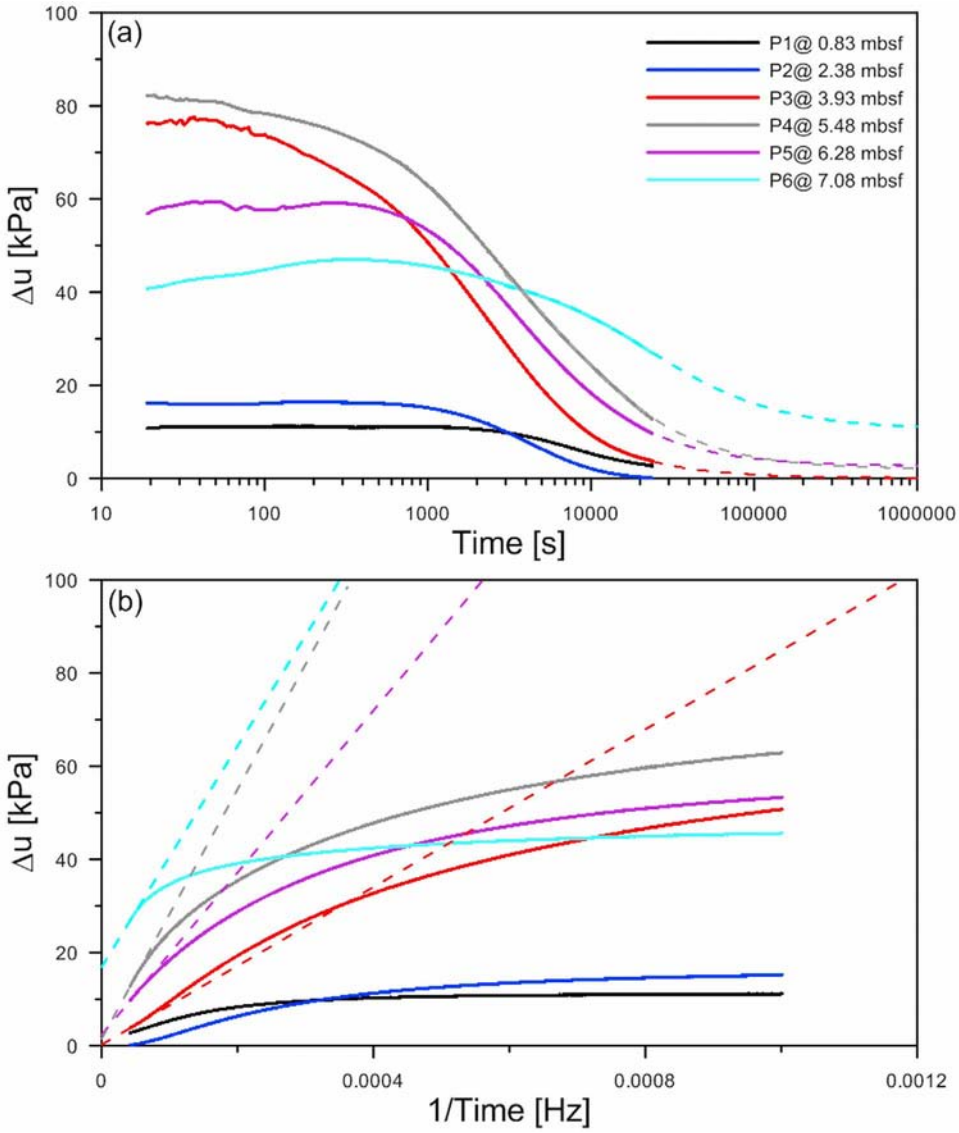

Figure 11. Initial impulsion overpressure and dissipation of the pore water pressure Δu (pore water pressure above the hydrostatic one) at six different levels generated by the piezometer PZY01 penetration (P1: 0.83 mbsf, P2: 2.38 mbsf, P3: 3.93 mbsf, P4: 5.48 mbsf, P5: 6.28 mbsf and P6: 7.08 mbsf). (a) Pore pressure versus time with equilibrium pore pressure extrapolated using *Burns and Mayne* [1998] method (dashed curves) and (b) pore pressure versus 1/time with equilibrium pore pressure extrapolated using *Davis et al.* [1991] method (dashed lines).

Figure 6. Core CS01 was recovered from an area characterized by low interval *P* wave velocity anomalies (from 3-D interval velocity analysis; Figure 2). Gas hydrates were absent from the CS01 core but some patches of gas exsolution along the core indicate the presence of some dissolved gas in the sediment pore water below 2 m. The consequence of the gas exsolution occurring in CS01 was an important decrease of the mass-density (Figure 6a), the lost of the *P* wave signal due to the presence of free gas (Figure 6b), and an important decrease of the shear strength (Figure 6c), and a important increase of the water content (Figure 6d). For some of the recovered cores, geochemical analyses with a determination of the gas compositions and concentrations were done using the headspace technique. Geochemical data are presented in Table 1 showing a gas composition of mainly methane and very low concentration of ethane for cores KSF20 and KSF37.

4.2. Piezocone Data and Detection of Gas Hydrates

[30] Piezocone measurements carried out by *Sultan et al.* [2007] show that the distinction between gas hydrates and carbonate concretions can be done thanks to the excess spore pressure generated during the rod penetration. Gas-hydrate-bearing sediments seem to be characterized by a specific type of piezocone data showing an important increase of the cone resistance accompanied by an important increase of the pore pressure. On the other hand, high cone resistance and low excess pore pressure (in some cases

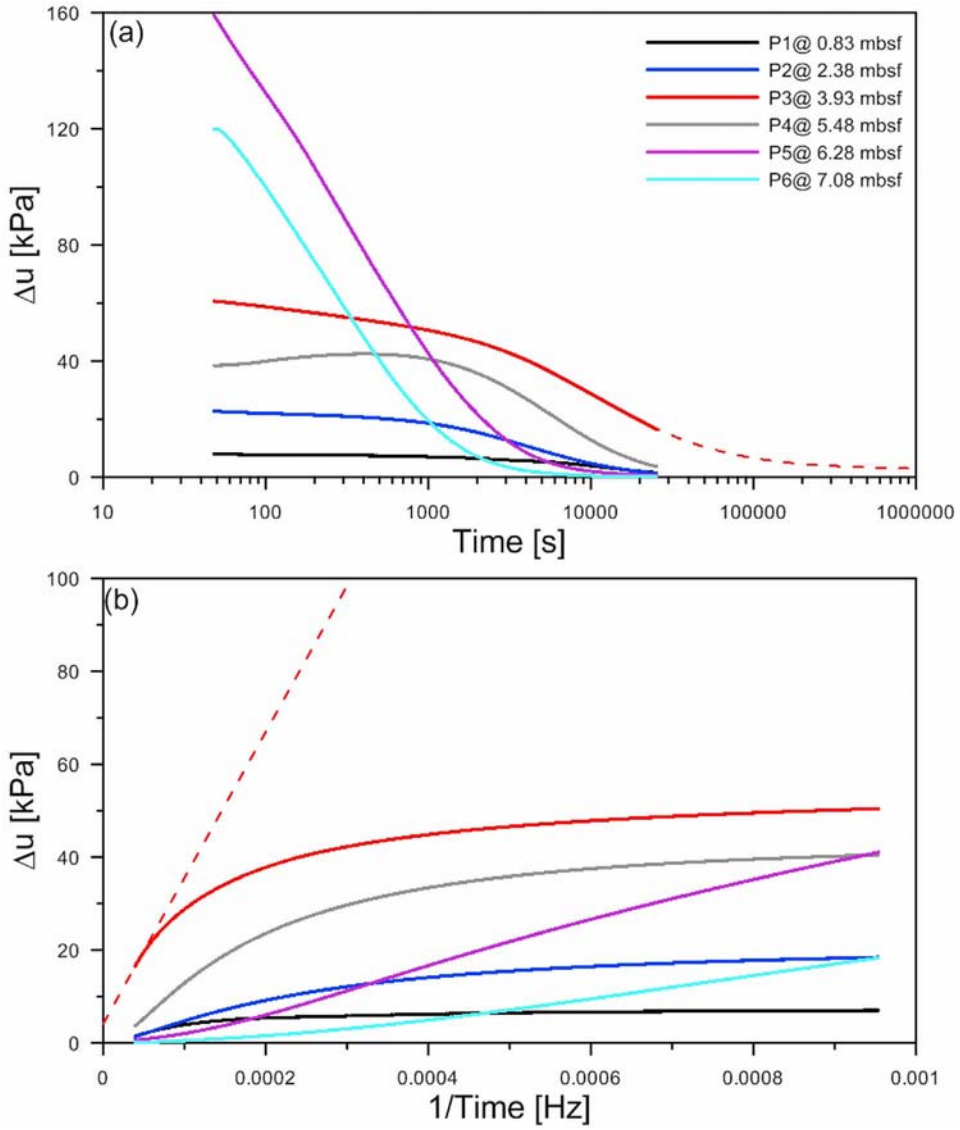

Figure 12. Initial impulsion overpressure and dissipation of the pore water pressure Δu (pore water pressure above the hydrostatic one) at six different levels generated by the piezometer PZY02 penetration (P1: 0.83 mbsf, P2: 2.38 mbsf, P3: 3.93 mbsf, P4: 5.48 mbsf, P5: 6.28 mbsf and P6: 7.08 mbsf). (a) Pore pressure versus time with equilibrium pore pressure extrapolated using *Burns and Mayne* [1998] method (dashed curves) and (b) pore pressure versus 1/time with equilibrium pore pressure extrapolated using *Davis et al.* [1991] method (dashed lines).

lower than the hydrostatic one) is generated during piezocone penetration through carbonate concretions layers [*Sultan et al.*, 2007].

[31] In situ piezocone data carried out in 2004 (NERIS cruise) were acquired from the southwestern part of the study area (pockmark B and C) and were presented and discussed by *Sultan et al.* [2007]. In 2008, the set of piezocone data was completed by acquiring piezocone data from the pockmark A (Figure 2; CPT02S01 to CPT02S09) and pockmark C (Figure 3; CPT04S02 to CPT04S05).

4.2.1. Pockmark A

[32] Figure 7 shows the cone resistance versus depth obtained from the nine sites (CPT02S01 to CPT02S09) located within and surrounding the pockmark A. For the first two sites (CPT02S01 and CPT02S02) the cone resistance increases linearly with depth showing the presence of homogeneous sediment, while the seven other piezocone tests carried out within the pockmark A show several important increase of the cone resistance (peaks) indicating the presence of stiff materials. Six CPTU acquired from the pockmark A are characterized by an early refusal at depth between 4.2 and 17.5 m (CPT02S03, CPT02S04, CPT02S05, CPT02S06, CPT02S07, and CPT02S09). CPT02S08 site is the only one where the piezocone rod was able to cross stiff materials (between 7.2 and 16 m) without early refusal.

[33] Figure 8 shows the excess pore pressure versus depth acquired from the nine sites (CPT02S01 to CPT02S09) located within and surrounding the pockmark A. The first two sites (CPT02S01 and CPT02S02) show once again the behavior of homogeneous sediments with a linear increase

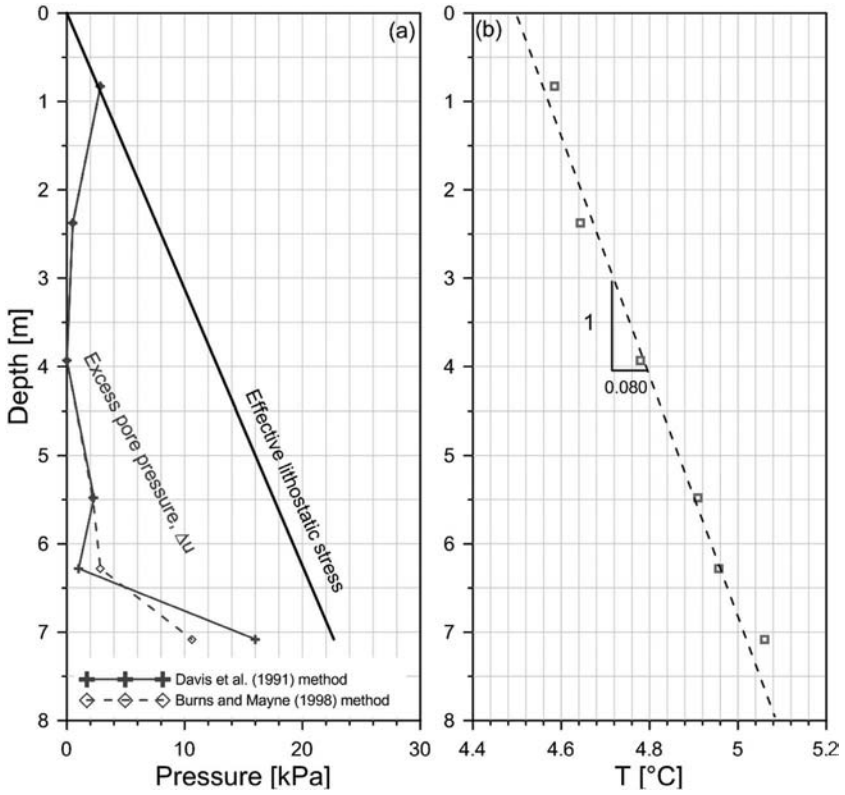

Figure 13. (a) Excess pore pressure at equilibrium obtained from *Davis et al.* [1991] and *Burns and Mayne* [1998] methods compared to the effective lithostatic stress profile and (b) temperature versus depth at site PZY01.

of the pore pressure with depth. The seven other sites (CPT02S03, CPT02S04, CPT02S05, CPT02S06, CPT02S07, CPT02S08, and CPT02S09) show that the cone resistance peaks presented in Figure 7 are also characterized by high excess pore pressure indicating the presence of gas hydrates at several depths within the pockmark A. CPT02S08 profile indicates that the rod has crossed an area where gas hydrates are present between 7.2 and 17 m. Comparison between recovered gas hydrate by coring (KS21, KSF23, and CS02), velocity anomalies derived from the D-stack analysis (Figure 2 and Figure 3), and in situ piezocone data show for the pockmark "A" good overall agreement between those different sets of data with the exception of CPT02S03 and CPT02S08. For both sites CPT02S03 and CPT02S08, D-stack *P* wave velocities over the first two reflectors (at 15 m and between 15 and 30 m below the seafloor) indicate the presence of normal sediments while the in situ piezocone data show several peaks with an early refusal for CPT02S03. For CPT02S08 site, this disagreement between piezocone data and *P* wave velocity is more likely related to the low gas-hydrate concentration and thickness at the periphery of pockmark A.

4.2.2. Pockmark C

[34] Figure 9 shows the cone resistance versus depth obtained from the eight sites (CPT04S02 to CPT04S05 and PM27A, PM33A, PM33B, and PM33C) located within and surrounding the pockmark C (for location see Figure 3). All CPTU tests presented in Figure 9 except CPT04S05 have undergone an early refusal at depth between 4.8 and 28.4 m. Most of the cone resistance peaks presented in Figure 9 correspond to high excess pore pressure measured during CPTU rod penetrations (Figure 10). Once again, the simultaneous increase of the cone resistance and the excess pore pressure is most likely an indication of the presence of gas hydrates. Figure 7 to Figure 10 indicate an important heterogeneous distribution of the gas hydrates within pockmarks A and C. The top of the gas hydrate occurrence zone (TGHOZ) at site PM27A was met at around 3 m below seafloor (mbsf), while at the adjacent site PM33B, the hydrate was discovered below 6 mbsf. For the pockmark A, the TGHOZ is at around 5.3 mbsf at CPT02S04 and is at around 3.4 mbsf at the nearby site CPT02S05.

[35] Comparison between recovered gas hydrate by coring (KS17, KSF19, KSF20, KS36, and KSF37), velocity anomalies derived from the D-stack analysis, and in situ piezocone data shows for the pockmark C good overall agreement between those different sets of data with the exception of CPT04S04.

4.3. In Situ Pore Pressure Data

[36] Figure 11 and Figure 12 present the initial impulsion overpressure and dissipation during 6 h of the pore water pressure above the hydrostatic one (Δu) at six different levels generated by the impact of piezometers at sites PZY01 and PZY02 in pockmark A. The equilibrium pressures (when it is not reached) are extrapolated using *Burns and Mayne* [1998] method (dashed curves in Figure 11a and Figure 12a) and the technique developed by *Davis et*

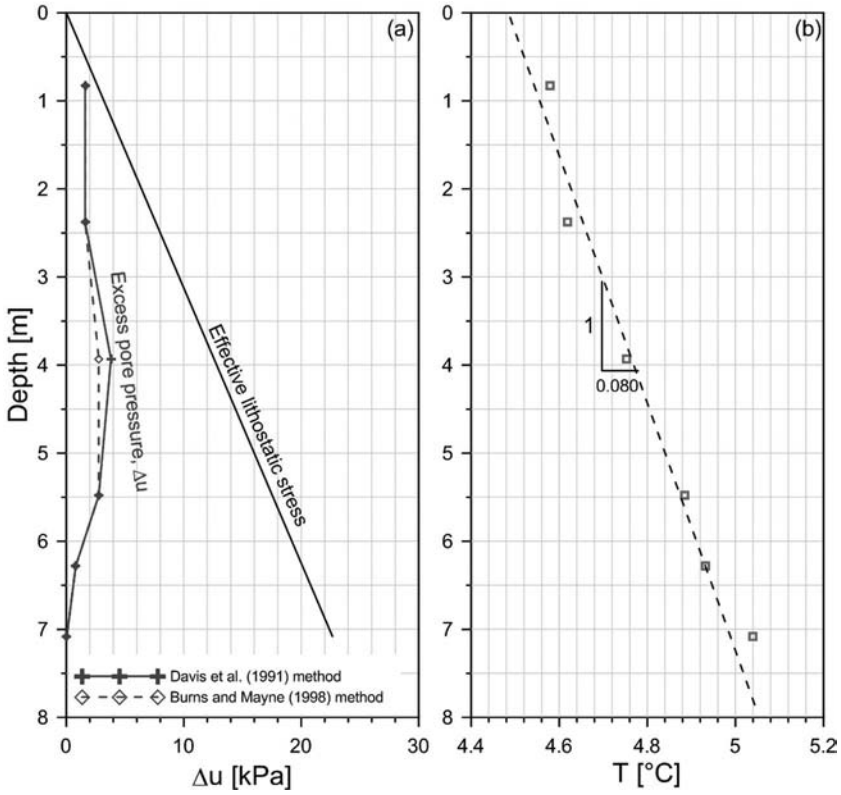

Figure 14. (a) Excess pore pressure at equilibrium obtained from *Davis et al.* [1991] and *Burns and Mayne* [1998] methods compared to the effective lithostatic stress profile and (b) temperature versus depth at site PZY02.

al. [1991] and *Fang et al.* [1993] by plotting the pressure record versus the reciprocal of time and extrapolated to 1/time = 0 (dashed lines in Figure 11b and Figure 12b).

[37] It is interesting to mention that for PZY02 the equilibrium pressure was reached for five of the sensors after 6 h measurements. Figure 13 shows the excess pore pressure with respect to the hydrostatic pressure and temperature at equilibrium versus depth at site PZY01. The effective lithostatic stress profiles presented in Figure 13 and Figure 14 are determined by integrating the submerged unit weight of the saturated sediments to the depth of interest. Figure 13a indicates an excess pore pressure between 11 kPa (around 50% of the effective lithostatic stress, equivalent to the parameter λ^* defined by *Flemings et al.*, 2008) and 16 kPa (around 70% of the effective lithostatic stress) at the base of the piezometer lance (7.08 mbsf). The piezometer data indicate that for the site PZY01, the excess pore pressure approaches the calculated hydro-fracturing pressure at around 7 mbsf. A high thermal gradient of 0.08°C/m was measured at PZY01 (Figure 13b). It is interesting to mention that sediments at PZY01 location are characterized by low D-stack *P* wave velocities over the first two reflectors presented in Figure 2.

[38] Figure 14 shows the excess pore pressure with respect to the hydrostatic one and temperature at equilibrium versus depth at site PZY02. Figure 14a shows a relatively low excess pore pressure (between 3 and 4 kPa, around 25% of the effective lithostatic stress) at the central part of the piezometer lance (3.93 mbsf) and no excess pore pressure at the base of the piezometer (7.08 mbsf). Once again it is important to mention that at PZY02 location, the D-stack *P* wave velocities indicate the presence of normal saturated sediments.

4.4. Shallow Sub-seafloor Geophysical Data

[39] Figure 15 and Figure 16 present two perpendicular VHR seismic profiles SY01-HR-PR01 and SY02-HR-PR07 acquired through pockmark A. The two VHR seismic profiles (Figure 15 and Figure 16) show the presence of two slight depressions surrounding the central part of the pockmark A. Both profiles show a significant contrast between high-amplitude chaotic facies in the central part of the pockmark and low-amplitude and subparallel reflectors at its periphery. These subparallel reflectors are characteristic of the presence of hemipelagic deposits as confirmed by core analysis (CS01). The two seismic profiles cross the central area of pockmark A where the presence of gas hydrates was suspected from the *P* wave velocity anomalies (Figure 2) and in situ piezocone data (blue areas in Figure 15) and confirmed by coring (CS02, KS21, and KS23; Figure 16). Figure 16 shows once again a significant contrast between high-amplitude chaotic facies from the central part of the pockmark and the much more continuous seismic facies of the surrounding sediment. This seismic profile crosses the central area of pockmark A where the presence of gas hydrates was suspected from the *P* wave velocity anomalies (Figure 2) and in situ piezocone data (blue areas in Figure 16) and confirmed by coring (CS02, KS21, and KS23).

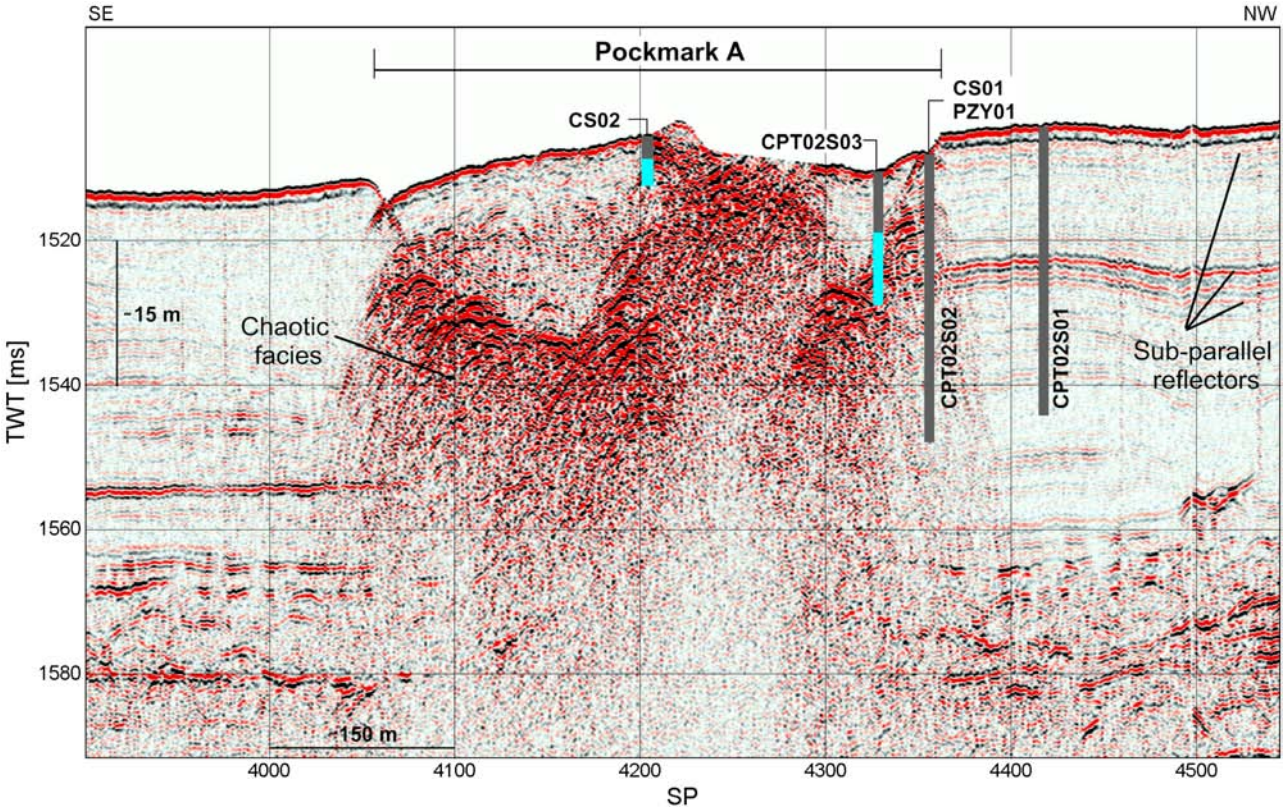

Figure 15. SYSIF seismic profile SY01-HR-PR01 through pockmark A showing a significant contrast between high-amplitude chaotic facies from the central part of the pockmark and the low-amplitude sub-parallel reflectors of the surrounding sediments. Piston cores (CS01 and CS02), piezometer (PZY01), and CPTU (CPT02S01, CPT02S02, CPT02S03 and CPT02S05) are projected onto the profile. For CPTU locations, shaded areas correspond to hemipelagic sediments, while the blue areas correspond to suspected gas hydrates.

[40] Figure 17 shows the seismic profile SY01-HR-PR02 acquired through pockmarks B and C. Pockmark B is marked by a pronounced depression of 30 m, and its internal structure is characterized by transparent to very low amplitude reflectors and, locally, chaotic low-energy facies. Pockmark C1 and C2 are marked locally by a very slight depression on the seafloor. Pockmark C1 shows a shallow heterogeneous high-amplitude chaotic facies. Pockmark C2 shows a relatively deep (the top at around 28 mbsf) high-amplitude chaotic facies in contrast with more continuous and low-energy seismic configuration of the upper sediments. This seismic profile crosses the limit of pockmark B and the central part of pockmark C1 where the presence of gas hydrates was suspected from the *P* wave velocity anomalies (Figure 3) and in situ piezocone data (blue areas in Figure 17) and confirmed by coring (KS17, KSF19, and KSF20).

[41] Figure 18 shows the seismic profile SY02-HR-PR03 acquired through pockmark C. Pockmark C3 shows an irregular topography and its internal structure is characterized by a variable seismic facies from very low amplitude reflectors to locally chaotic facies. This seismic profile crosses the border of pockmarks C1 and C3 where the presence of gas hydrates was suspected from the *P* wave velocity anomalies (Figure 4) and in situ piezocone data (blue areas in Figure 18) and confirmed by coring (KSF36 and KSF37).

5. Discussion

5.1. Morphology, Gas-Hydrate Distribution, and Sub-seafloor Features

[42] The seafloor features display different pockmark shapes and sizes (Figure 1): (1) a large-scale circular depression about 110 m deep and 700 m in diameter (pockmark D; Figure 1); (2) numerous small pockmarks line up along underlying southern major fault plane, thus suggesting the presence of migration pathway along this fault up to the seafloor (pockmarks crossing line L1; Figure 1), and (3) more irregular depressions on the seafloor, with a great variability in morphology, size (100–600 m in diameter) and acoustic characteristics. The size and distribution of this last type (type 3) of pockmark seems related to the occurrence of gas hydrates (example pockmarks A, B, and C in Figure 1).

[43] Detailed analyses of the interval *P*-wave seismic velocity field and piezocone measurements acquired from the study area were published in the paper by *Sultan et al.*

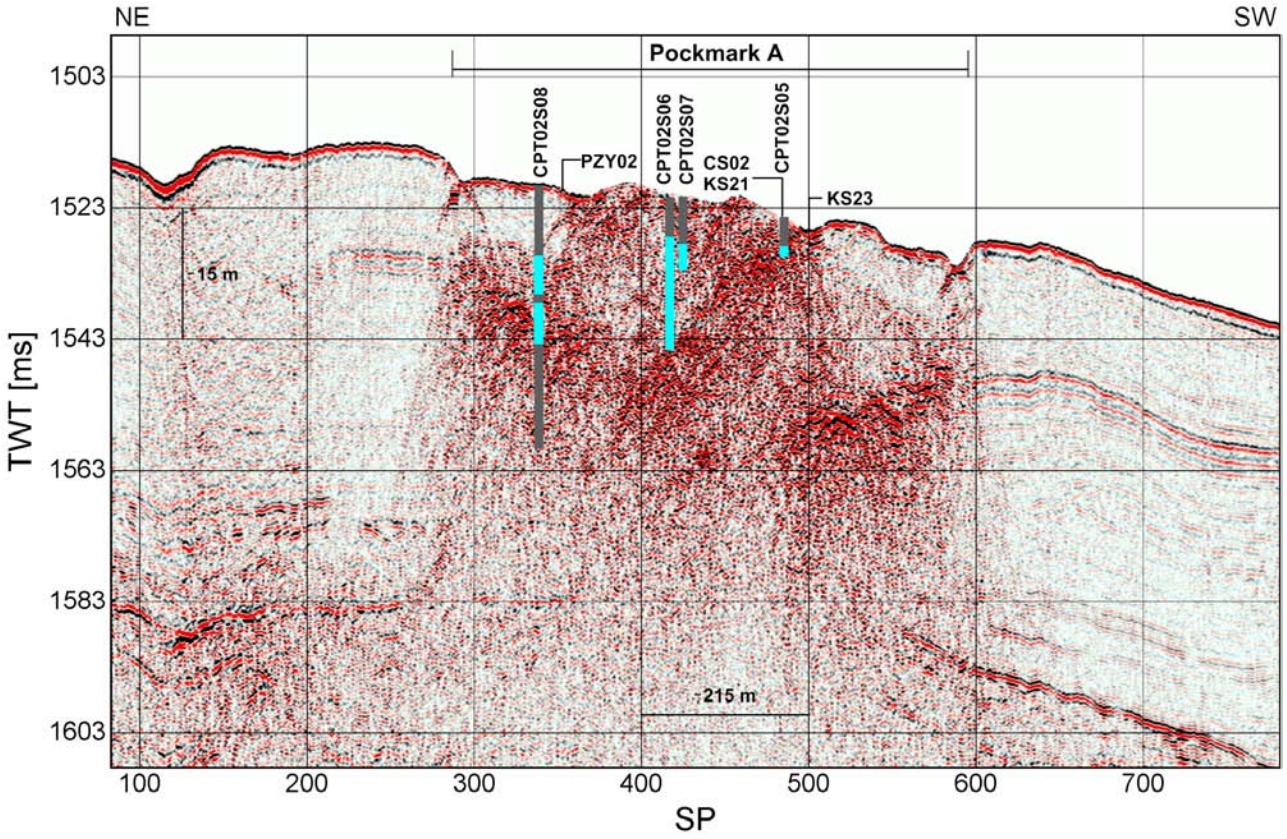

Figure 16. SYSIF seismic profile SY02-HR-PR07 through pockmark A showing once again a significant contrast between high-amplitude chaotic facies from the central part of the pockmark and the much more continuous seismic facies of the surrounding sediment. Piston cores (CS02, KS21 and KS23), piezometer (PZY02), and CPTU (CPT02S05, CPT02S06, CPT02S07 and CPT02S08) are projected onto the profile. For CPTU locations, shaded areas correspond to hemipelagic sediments, while the blue areas correspond to suspected gas hydrates.

[2007] and were used to determine the occurrence of gas hydrate within the studied pockmarks. Additional in situ geotechnical data recovered in 2008 (ERIG3D cruise) and presented in Figure 7 to Figure 10 bring further evidence of the presence of gas hydrate in the central part of the studied pockmarks. It is interesting to mention that for pockmark A (Figure 2), the in situ piezocone CPT02S8 has crossed the GHOZ suggesting that gas hydrate is more massive and deeper in the central part with respect to its periphery.

[44] Based on those different geophysical and geotechnical data, it is possible to define a typical internal architecture of the studied pockmarks where the gas hydrate in the central part of the structure with a flat or positive relief is surrounded by sediments characterized by a low *P* wave velocity and possibly overpressured as it was demonstrated at the PZY01 location. In-line (P1) and cross-line (P2) profiles (for location see Figure 1) extracted from a pseudo-3-D AUV seismic cube acquired over the entire northern pockmark are presented in Figure 19. A superficial collapse surrounding the GHOZ can be clearly observed from the two SBP profiles. Figure 19b shows the presence of a continuous reflector below the superficial depression. The continuity of this reflector indicates that the sediment deformations (ring shape; Figure 2) surrounding the central part of the northern pockmark are localized in the upper sedimentary layers and are not a direct consequence of deep depressions. Moreover, the identified fault in Figure 19b and Figure 20 suggest that the distribution of gas/fluid migration paths caused by pre-existing vertical weakness zones within the shallow sediments is at the origin of the gas-hydrate occurrence. Figure 20 shows a 3-D seismic profile crossing the pockmark A and confirms the two previous observations about the sediment collapse localized in the upper sedimentary layers and the presence of gas/fluid migration paths which are at the origin of the gas-hydrate occurrence within the pockmark A.

5.2. Pockmarks Evolution Versus Hydrate Dissolution: Qualitative Description

[45] Due to the pressures at water depths ≥ 1100 m, the low seafloor temperature (4°C), and the normal salinity, our working hypothesis is to consider gas-hydrate dissolution as the main mechanism for developing and maintaining pockmarks in the studied area rather than the gas-hydrate dissociation which is often considered as a mechanism of sediment deformation [e.g., *Carpenter*, 1981; *McIver*, 1982; *Kayen and Lee*, 1991]. Moreover, the heterogeneous morphology and development stages of these small depressions

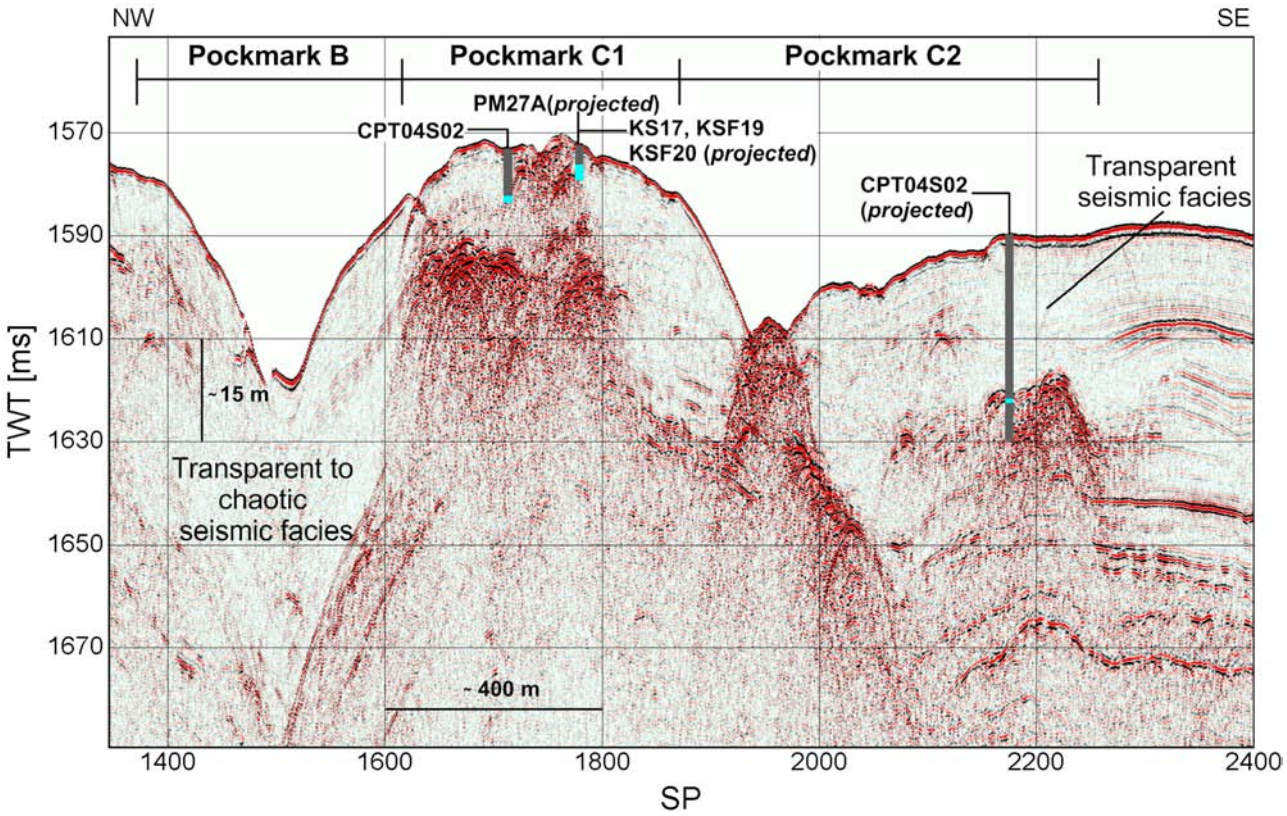

Figure 17. SYSIF seismic profile SY01-HR-PR02 through pockmarks B and C. Pockmark B is characterized by a reflection-free transparent zone to very low amplitude chaotic facies. Pockmark C-1 shows a shallow heterogeneous high-amplitude chaotic facies. Pockmark C-2 shows a relatively deep (the top at around 28 mbsf) high-amplitude chaotic facies in contrast with more continuous seismic facies of the upper sediment. Piston cores (KS17, KSF19 and KSF20) and CPTU (CPT04S02, CPT04S05, PM27A and PM33A) are projected onto the profile. For CPTU locations, grey areas correspond to hemipelagic sediments while the blue areas correspond to suspected gas hydrates.

should be related to a local process like dissolution rather than a regional one. The dissolution of the gas hydrates can be either generated by an increase of the gas solubility due to a decrease of the temperature conditions or by a decrease or the stop of the gas flow supplying the hydrated sediments. For the temperature and pressure conditions of the study area, a temperature decrease of around 5°C will lead to an increase of the methane solubility by around 10% (for methane solubility curves see for instance the work of *Davie et al.* [2004]) which will cause a limited dissolution of the hydrates. For the second case, the cease of the gas flow supplying the hydrated sediments will cause the complete disappearance of the gas hydrates.

[46] Even well within the hydrate stability field, deep-sea experiments carried out by *Rehder et al.* [2004] have demonstrated that gas hydrates dissolved by the contact with undersaturated water. *Rehder et al.* [2004] have shown that long-term survival of hydrate close to the seafloor must be sustained by sufficient supply of gas to maintain boundary layer saturation or to continuous hydrate growth. While this experimental observation was already well defined theoretically by *Egorov et al.* [1999], the consequence of such dissolution of gas-hydrate-bearing sediment in terms of sediment deformation and excess pore pressure remains at this moment experimentally unquantified.

[47] The formation of a ring depression around the GHOZ and its evolution as a function of hydrate formation and dissolution is tentatively presented in Figure 21a according to the following five phases:

[48] Phase 1: Upward migration of free gas and pore fluids saturated with dissolved gas through existing permeable fault systems. Free gas and gas-hydrate nucleation occur above a critical depth (gas exsolution level, GEL) where the decreased hydrostatic pressure would cause degassing and gas exsolution.

[49] Phase 2: After gas-hydrate nucleation, gas hydrates start to grow as a result of diffusion and suction of dissolved gas toward gas-hydrate particles. Expansion volume due to hydrate growth is accommodated by upper sediments compaction but also by uplift of the upper sedimentary layers. Although gas hydrate is presented schematically as a homogenous patch, in the study area, coring and in situ measurements have shown a great heterogeneity in gas-hydrate distribution.

[50] Phase 3: Gas hydrate must be sustained by a sufficient supply of gas to maintain gas saturation at the hydrate solid boundary. A decrease of fluid migration through fault

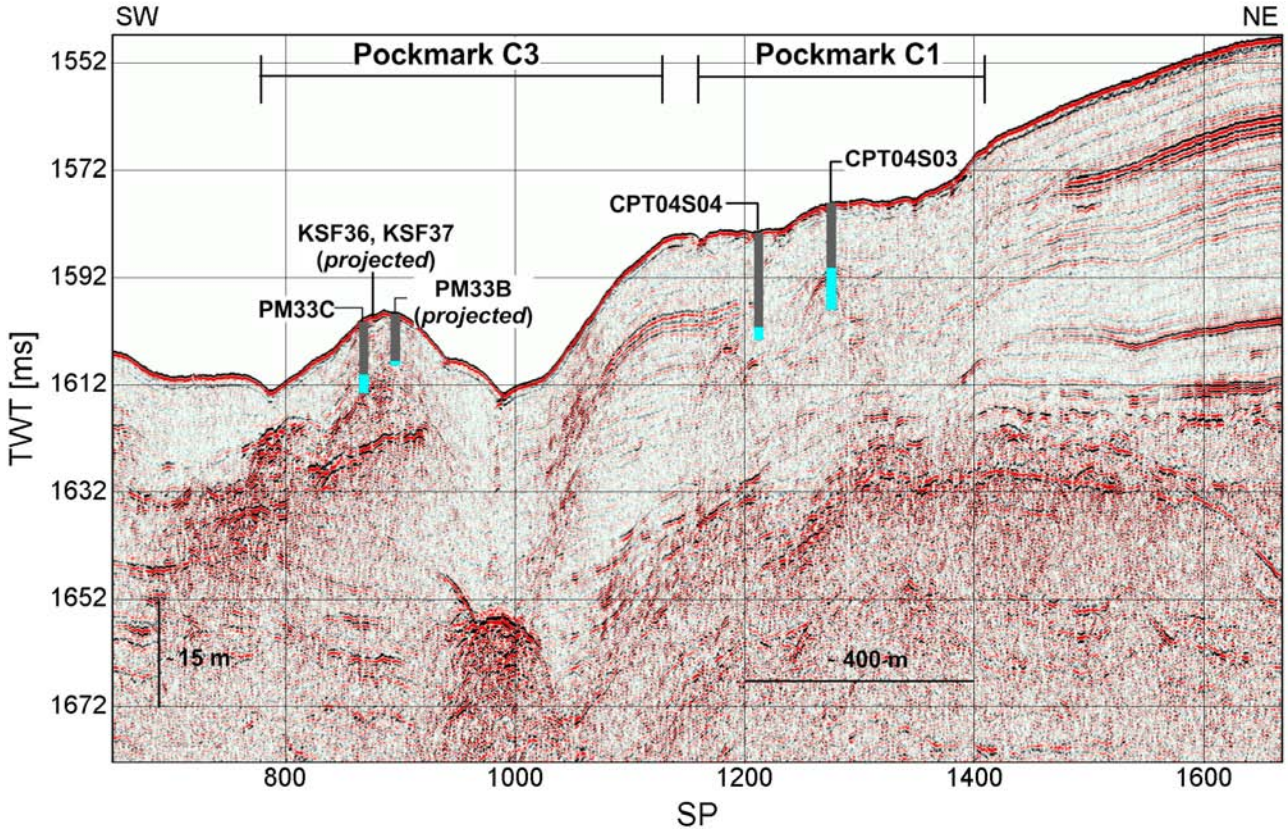

Figure 18. SYSIF seismic profile SY02-HR-PR03 through pockmark C. Pockmark C-3 is characterized by a reflection-free transparent zone to very low amplitude chaotic facies. Piston cores (KSF36 and KSF37), and CPTU (CPT04S03, CPT04S04, PM33B and PM33C) are projected onto the profile. For CPTU locations, shaded areas correspond to hemipelagic sediments, while the blue areas correspond to suspected gas hydrates.

systems could lead to a decrease in the gas content below saturation at the gas-hydrate boundary. In response, the solid hydrate at the boundary of the sediment-hosted gas hydrate is "dissolved" into a mixture of water and dissolved gas. Hydrate dissolution and sediment collapse increase then the pore pressure which subsequently is expected to alter locally the fluid flow regime.

[51] Phase 4: Hydrate dissolution and the collapse and compaction of the gas-hydrate-bearing sediment generates excess pore pressure. The fluid flow generated by the excess pore pressure gets around the gas-hydrate-bearing sediment because of the low permeability of the medium. The loss of the massive hydrate by dissolution at the border of the solid hydrate and the pore pressure dissipation are accompanied by a decrease of the sediment porosity at the border of the GHOZ and a deepening of the depression surrounding and above the sediment hosted gas hydrates.

[52] Phase 5: The last stage of the pockmark evolution corresponds to the disappearance of the solid hydrate and the cease of fluid activities.

[53] The hypothesis concerning the presence of several pockmarks at different stages of maturation in a relatively localized study zone and the high quantity of acquired geophysical data in the area let us expect the presence of geophysical facies matching with the five different phases of pockmark formation process described in Figure 21a. This was confirmed by considering the four different SYSIF seismic profiles acquired from the three studied pockmarks and presented in Figure 15 to Figure 18. Figure 21b presents five different facies showing similarities with the five sketches presented in Figure 21a: gas-hydrate formation (phase 1,- eastern border of pockmark C2), hydrates growth and uplift of the upper sedimentary layers (phase 2, pockmark C1), gas-hydrates dissolution at the boundary of the sediment-hosted gas-hydrate-inducing sediment collapse and the ring formation (phase 3, pockmark A), evolution of the ring with deepening of the depression surrounding and above the sediment hosted gas hydrates (phase 4, pockmark C2), and finally the last stage of the pockmark evolution corresponding to the disappearance of the solid hydrate (phase 5, pockmark B).

5.3. Pockmarks Evolution Versus Hydrate Dissolution: Modeling

[54] In order to verify theoretically our working hypothesis concerning hydrate dissolution and the pockmark formation and evolution, a numerical calculation was carried out. The aim is to define the gas-hydrate dynamics from pockmark A in the northern part of the study area (Figure 2) under an important decrease of the gas concentration underneath the GHOZ.

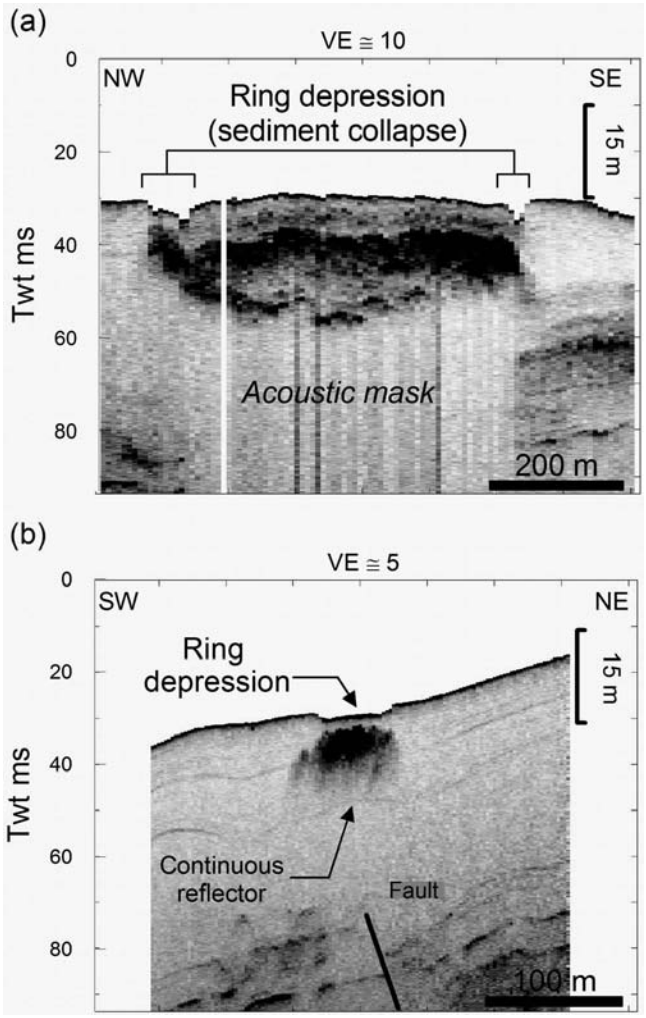

Figure 19. Pockmark A: (a) In-line P1 and (b) cross-line P2 profiles (for location see Figure 1) extracted from a pseudo 3D *AUV* seismic cube [*Georges and Cauquil*, 2007 - Ifremer processing] acquired over the entire northern pockmark (Figure 2-a). From line P2, note the continuous upper reflectors in contrast with basal reflectors.

5.3.1. Initial and Boundary Conditions

[55] For the 2-D numerical modeling, the calculation domain was divided into six different layers, and the faults zone observed from the 3-D seismic data (Figure 20) was considered as the source of upward free gas circulation and consequently of gas- hydrate formation. The 2-D cross section presented in Figure 22a has a length of around 0.7 km.

[56] For initial conditions, we imposed at the base of the layer 6 in the faults area (over 200 m) a high concentration of methane (0.005 mol CH_4/H_2O mol ≈ 10% of hydrate fraction) which is the only gas forming the gas hydrates in the pockmark A (Table 1). At this initial stage, the presence of the free gas in the faults zone are considered to take place through different gas transport processes (diffusion and advection through faults) leading to a constant methane concentration. The methane concentration surrounding the faults area is determined using Fick's law. The temperature (4.08°C at the seafloor and a thermal gradient of 75°C/km at the base of the calculation domain; *Sultan et al.*, 2007) and salinity (34‰, *Caprais and Pignet*, 2009) conditions were considered constant for the entire calculation. Porosity values were obtained from the compressibility curves obtained from oedometer tests (data from *Sultan et al.* [2007]). Initial methane concentration, temperature, and porosity profiles from inside and outside of the GHOZ are presented in Figure 22b, 22c, and 22d. The methane concentration includes the dissolved gas and the gas trapped in the hydrate phase above the BGHSZ and the free and dissolved gas below the BGHSZ. The gas hydrates which impede the normal consolidation of the sediment lead to high porosity in the GHOZ. The hydraulic diffusivity D_H which is a key parameter in the Darcy's equation is presented in Figure 22d as a function of depth from inside and outside the GHOZ. The presence of gas hydrates decreases significantly the hydraulic diffusivity values.

[57] In Figure 23 the initial iso-contours of the methane concentration, hydrate fraction, and porosity are presented. The gas source position and distribution at the base of faults

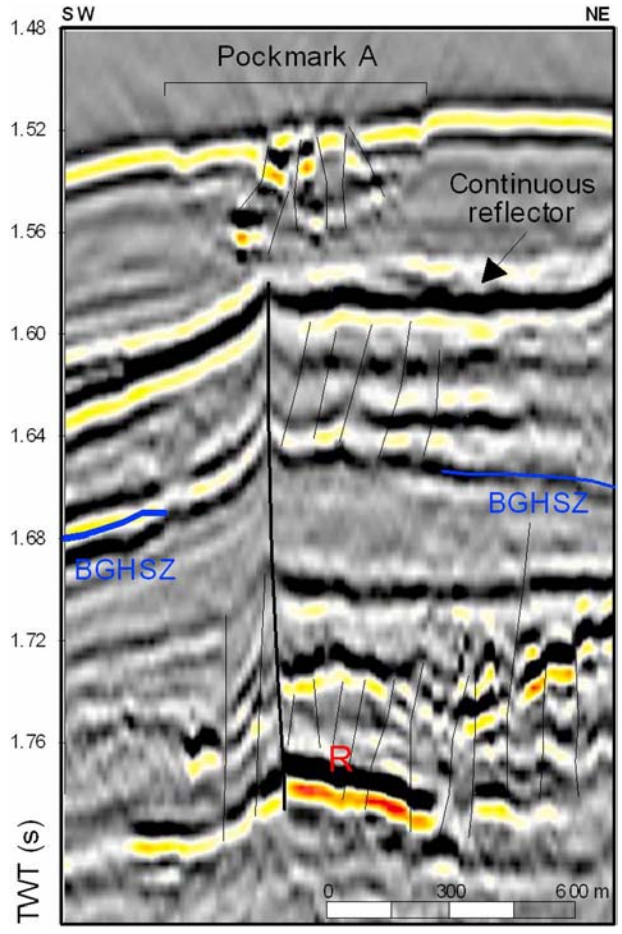

Figure 20. A NE-SW 3D seismic profile crossing the pockmark "A" along the SY02-HR-PR07 position presented in Figure 2. The sediment collapse is localized in the upper sedimentary layers and several gas/fluid migration paths (faults) are localized underneath the pockmark A.

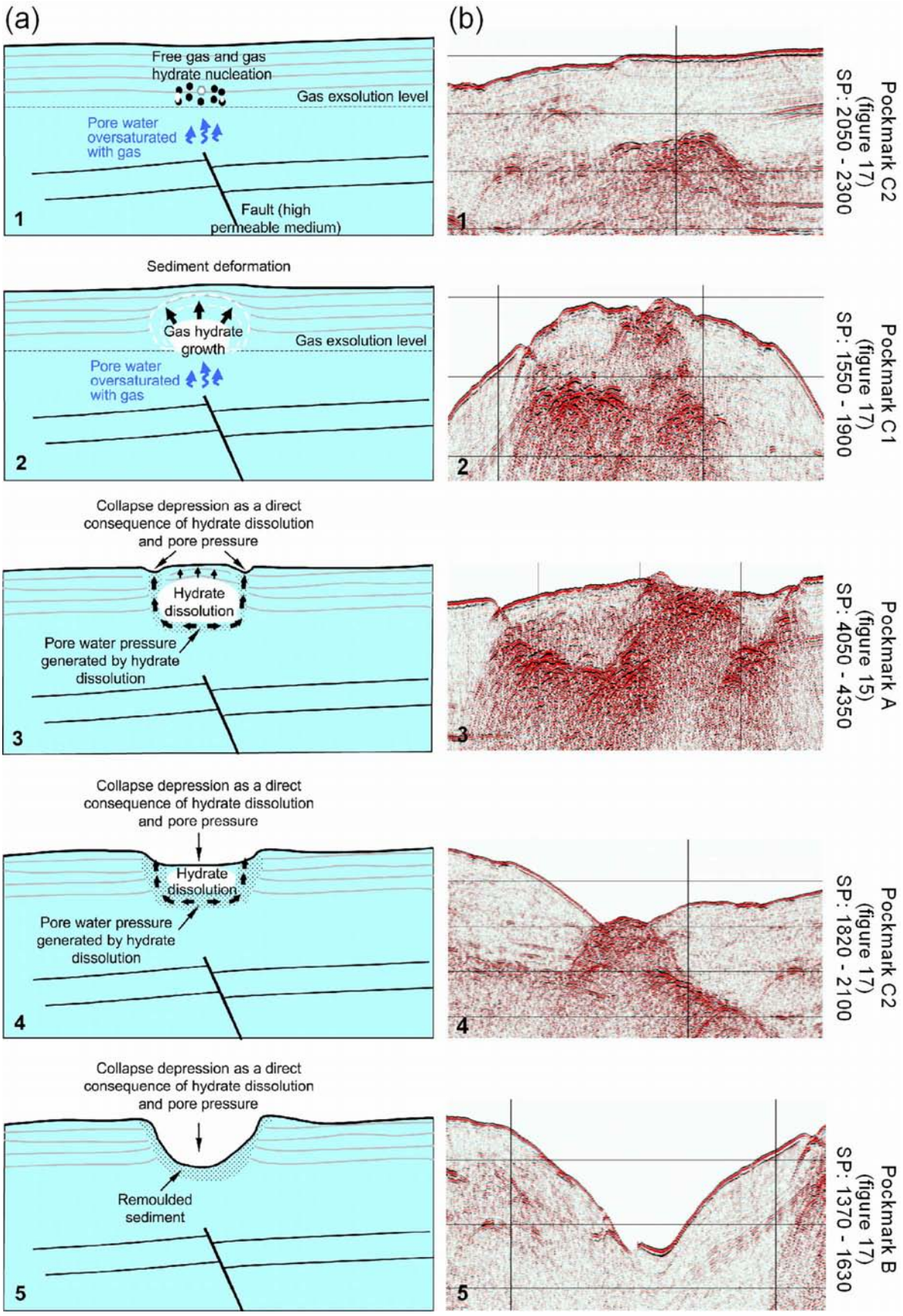
(a)
(b)
Free gas and gas hydrate nucleation
Gas exsolution level
Pore water oversaturated with gas
Fault (high permeable medium)
1
Pockmark C2 (figure 17) SP: 2050 - 2300
Sediment deformation
Gas hydrate growth
Gas exsolution level
Pore water oversaturated with gas
2
Pockmark C1 (figure 17) SP: 1550 - 1900
Collapse depression as a direct consequence of hydrate dissolution and pore pressure
Hydrate dissolution
Pore water pressure generated by hydrate dissolution
3
Pockmark A (figure 15) SP: 4050 - 4350
Collapse depression as a direct consequence of hydrate dissolution and pore pressure
Hydrate dissolution
Pore water pressure generated by hydrate dissolution
4
Pockmark C2 (figure 17) SP: 1820 - 2100
Collapse depression as a direct consequence of hydrate dissolution and pore pressure
Remoulded sediment
5
Pockmark B (figure 17) SP: 1370 - 1630

Figure 21

zone was taken to fit the high amplitude reflector marked *R* in Figure 23a. For the initial considered gas concentration, the maximum hydrate fraction was calculated equal to 10% at the base of the GHOZ. The presence of the gas hydrates is at the origin of the high porosity shown in Figure 23d.

5.3.2. Numerical Results

[58] At time 0+, the methane concentration was reduced drastically (0.00001 mol CH_4/H_2O mol) at the base of layer 6 (gas source level). In the following, the only process controlling the methane concentration is the diffusion through the Fick's law and the methane diffusivity coefficient taken equal to 10^{-12} m^2/s [*Bigalke et al.*, 2009]. The pore pressure distribution is calculated using the Darcy's law and the hydraulic diffusivity which depends on the porosity and the hydrate fraction.

[59] Two thousand years after the decrease in methane concentration, the decrease of the methane concentration (Figure 24a) in the GHOZ was enough to dissolve significantly the gas hydrates (Figure 24b). The maximum hydrate fraction decreases to 0.085 in the central part of the GHOZ. The gas-hydrates dissolution occurs mainly at the upper boundary of the GHOZ (Figure 24a). This dissolution process and the subsequent compaction of the gas-hydrate-bearing sediment generate an important increase in pore pressure reaching in the upper boundary of the GHOZ the pore pressure needed to generate hydro-fracturing (Figure 24c). The dashed area in Figure 24c corresponds to the hydro-fractured zone. The iso-contours of the excess pore pressure and the fluid flow (vector field) presented in Figure 24-d show that the source of the excess pore pressure is localized in the low-permeability gas-hydrate-bearing sediments.

[60] Four thousand years after the decrease in methane concentration at the base of layer 6, the dissolution of the gas hydrates continues to occur mainly at the boundary of the GHOZ (Figure 25a and 25b). The pore fluid generated by hydrate dissolution and sediment compaction exceeds once again the fluid pressure needed to generate hydro-fracturing inducing an expansion of the hydro-fractured area (dashed area in Figure 25c). The source of the excess pore pressure is localized in the low-permeability gas-hydrate-bearing sediments (Figure 25d).

[61] Figure 26 presents the calculation results 8000 years after the decrease in methane concentration. Figure 26a shows the iso-contours of the methane concentration. The gas-hydrates dissolution (Figure 26a) is accompanied by the expansion of the hydro-fractured area which surrounds the central hydrated zone (dashed area in Figure 26c). The source of the excess pore pressure is still localized in the low permeability gas-hydrate-bearing sediments (Figure 26d).

[62] For the two first calculations, the fluid flow distribution around the low-permeable hydrated medium (Figure 24d and Figure 25d) is comparable to the geophysical facies observed in Figure 19a. Moreover, the excess pore pressure between 11 and 16 kPa measured at the base of PZY01 (Figure 13) suggests that the formation process of the pockmark A is still in an initial stage phase where the excess pore pressures are limited to the boundary of the GHOZ.

[63] The iso-contours of the hydraulic diffusivity presented in Figure 27 illustrate the evolution of the hydro-fractured zone during the dissolution of the gas hydrates. The hydraulic diffusivity of the sediment depends on the hydrate fraction but also on the hydro-fracturing level of the medium. Figure 27 shows the evolution of the deformed sediments surrounding the hydrated sediment with an initial depression at the upper border of the hydrated sediment (Figure 27a) similar to the morphology of pockmark A (Figure 1). This initial ring depression is followed by an important extension of the fractured area which after 8000 years surrounds completely the inner sediments rich in gas hydrates.

5.3.3. Calculation Uncertainties

[64] While the presence of gas hydrates was assumed based on in situ piezocone measurements and VHR seismic data and was established by coring, the gas-hydrate concentrations and fractions were considered to fit with the interval velocity values derived from 3-D seismic data. The use of the *P* wave velocity values alone to quantify the hydrate fractions is not precise since other materials like carbonate concretions or rocks are also characterized by high *P* wave velocities. In some cases, the coexistence of gas hydrate and carbonate is also possible since both carbonate and cemented sediment may result from methane production and gas-hydrate decomposition. Therefore, an important source of uncertainty in this work is related to the determination of gas-hydrate fractions.

[65] The second source of uncertainty is related to the important numbers of key parameters (mineralogy, porosity, permeability, compressibility, thermal and hydraulic diffusivities, gas concentrations, salinity, etc.) used in the numerical calculation and which are essential in the hydrate dissolution process. The dependence of those key parameters on the hydrate concentration and distribution makes the uncertainty in this kind of calculation significant.

[66] The third source of uncertainty is linked to the hydraulic fracturing process generated by excess pore pressure. For gas-hydrate-bearing sediments, the tensile strength depends strongly on the hydrate concentration and may raise significantly its value.

[67] Finally, the evolution time scale of this type of pockmark depends strongly on several unidentified parameters (e.g., the gas-hydrate concentration and distribution in the area, the permeability and the mechanical behavior of the gas-hydrate-bearing sediment, and the kinetics of the

Figure 21. (a) Sketch of five different phases of pockmark evolution during hydrate formation and dissolution. Dynamic of free gas and fluid saturated by dissolved gas flow through fault systems is the main cause of the hydrate formation and dissolution and the subsequent sediment deformation and pockmark evolution. (b) Blowup of five different SYSIF seismic profiles taken from the three studied pockmarks showing similarities between the sketch and observed facies (phase 1: SY01-HR-PR02 and shot point (SP) P 2050 to 2300; phase 2: SY01-HR-PR02 and SP 1550 to 1900; phase 3: SY01-HR-PR01 and SP 4050 to 4350; phase 4: SY01-HR-PR02 and SP 1820 to 2100 and phase 5: SY01-HR-PR02 and SP 1370 to 1630).

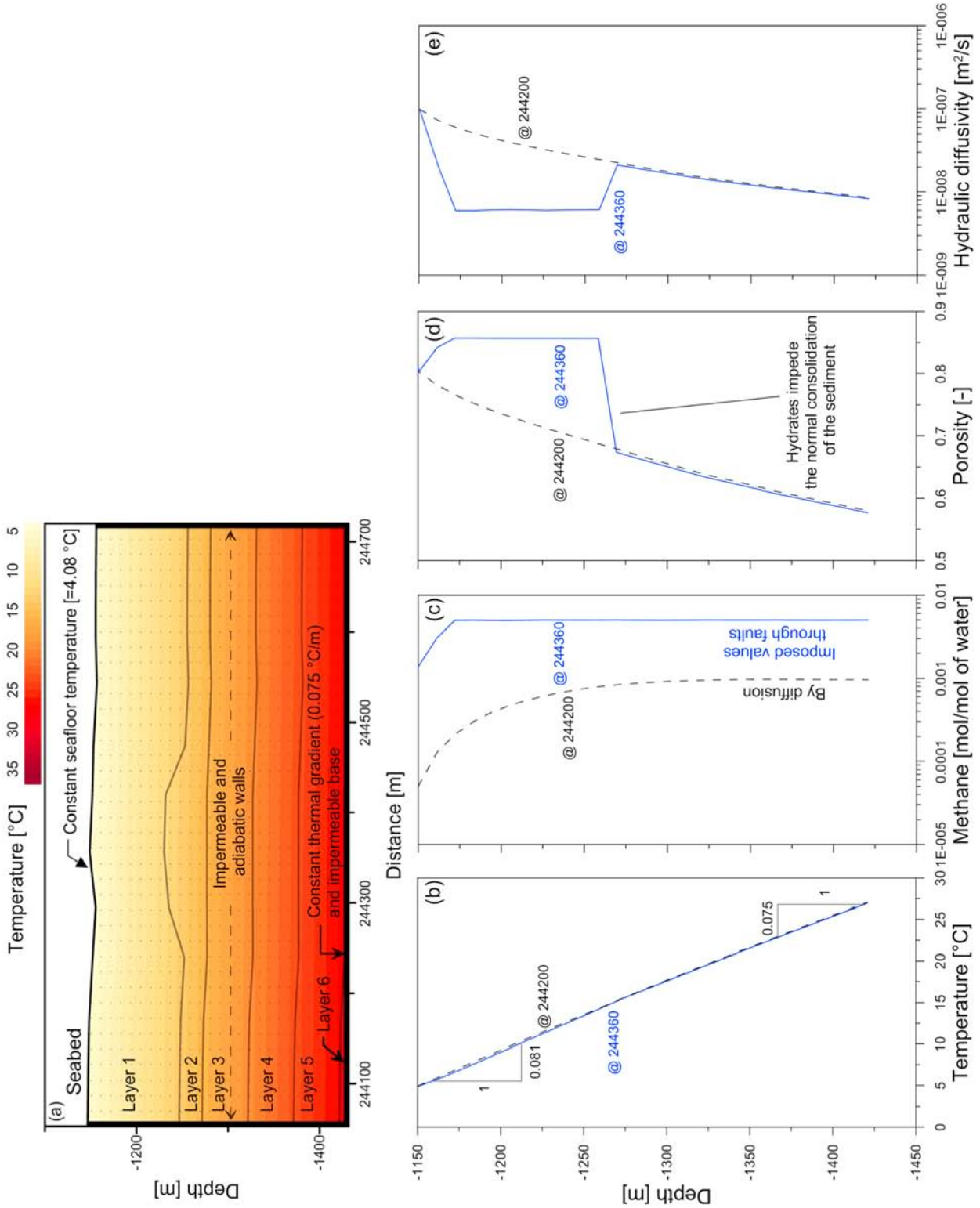
(a)
Seabed
Constant seafloor temperature [=4.08 °C]
Layer 1
Layer 2
Layer 3
Layer 4
Layer 5
Layer 6
Impermeable and adiabatic walls
Constant thermal gradient (0.075 °C/m) and impermeable base
Temperature [°C]
Depth [m]
Distance [m]
(b)
(c)
(d)
(e)
@ 244200
@ 244360
0.081
0.075
1
By diffusion
Imposed values through faults
Hydrates impede the normal consolidation of the sediment
Porosity [-]
Methane [mol/mol of water]
Hydraulic diffusivity [m²/s]

Figure 22

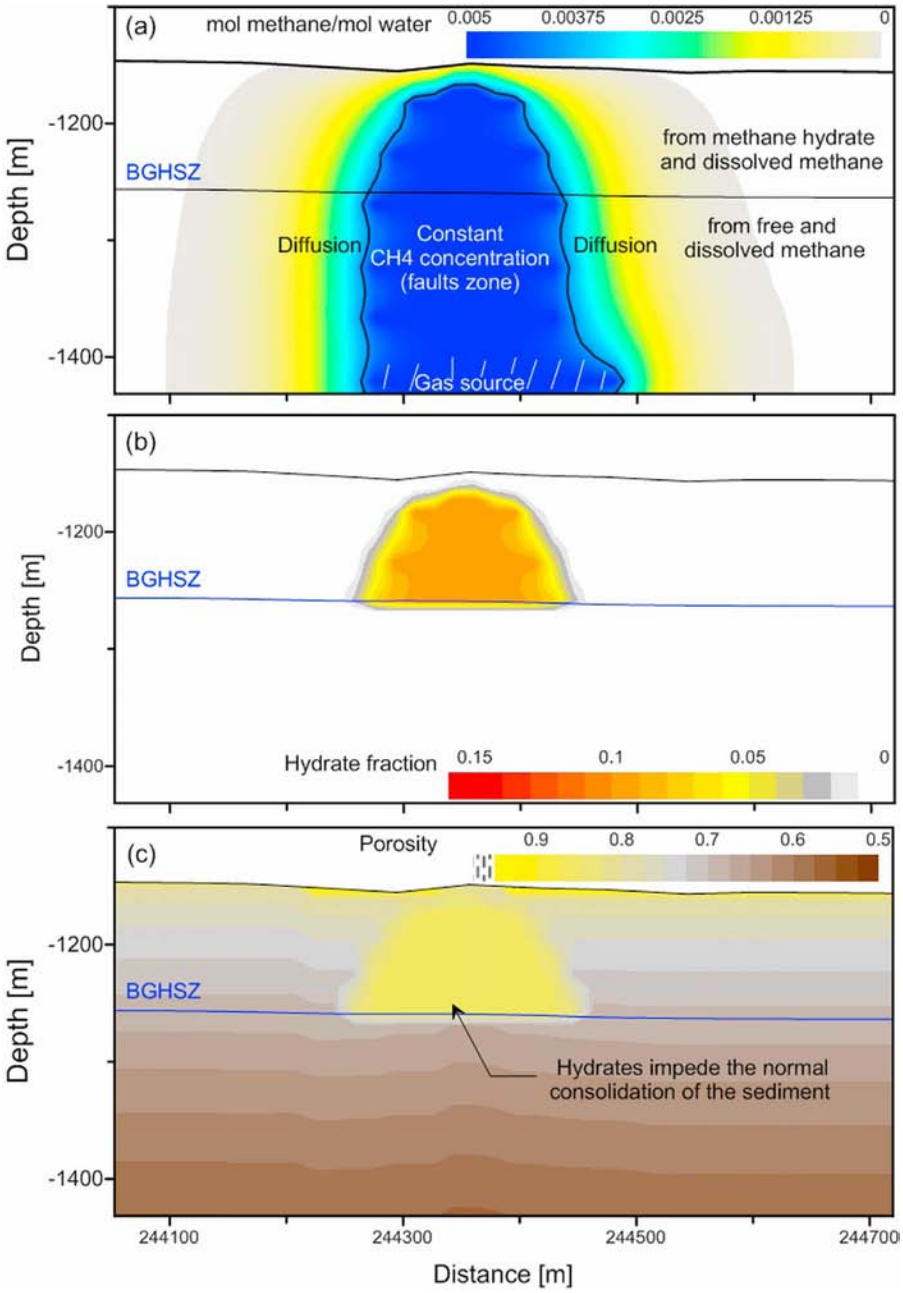

Figure 23. Initial (at time 0) iso-contours of (a) the methane concentration, (b) the gas-hydrate fraction, and (c) the porosity. At time 0, the methane concentration is considered constant in the faults zone and was calculated in the surrounding area using Fick's law. The maximum gas-hydrate fraction was found equal to 0.1. The presence of the gas hydrates impede the normal consolidation of the sediment (high porosity observed in the lower diagram).

Figure 22. (a) Model geometry, initial and boundary conditions. (b) Initial temperature profile located inside (@244360) and outside (@244200) the GHOZ. (c) initial methane concentration profile located inside (@244360) and outside (@244200) the *GHOZ*. The initial methane concentration in the faults zone is considered constant and taken equal to 0.005 mol of methane per mol of water. This methane concentration includes the dissolved gas and the gas trapped in the hydrate phase above the BGHSZ and the free and dissolved gas below the BGHSZ. (d) Initial porosity profile located inside (@244360) and outside (@244200) the GHOZ. The gas hydrates impede the normal consolidation of the sediment leading to higher porosity in the GHOZ. (e) Two hydraulic diffusivity D_H profiles located inside (@244360) and outside (@244200) the GHOZ. The presence of gas hydrates decreases significantly D_H.

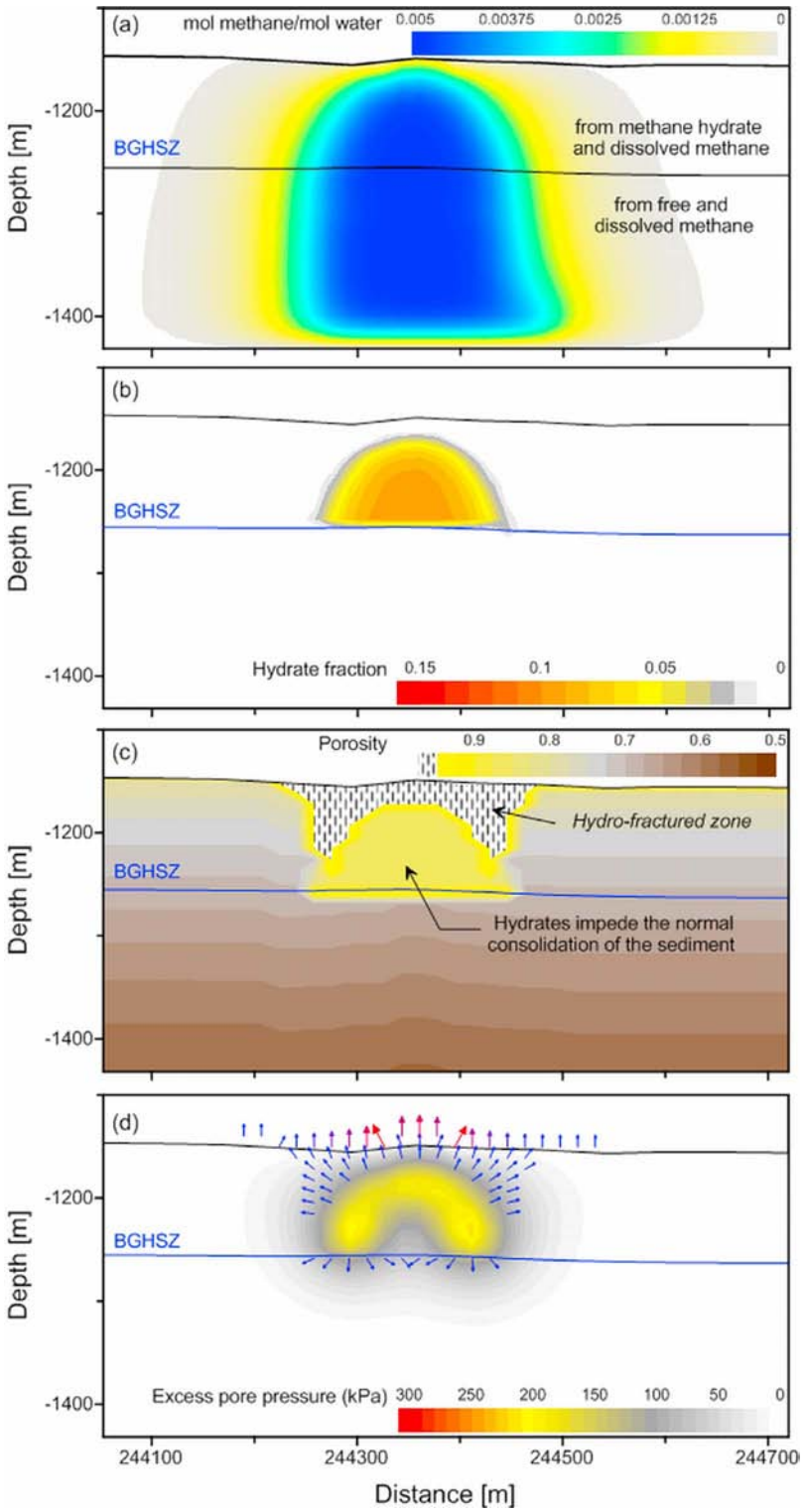

Figure 24. Modeling of the dynamic of the gas hydrate and the dissolution process related to the decrease of the methane concentration at the base of calculation domain. Iso-contours of (a) the methane concentration, (b) the gas-hydrate fraction, (c) the porosity, and (d) the excess pore pressure (contours, measured in kilopascals) at calculation time step of 2000 years. The fluid flow (vector field) is projected on the lower diagram.

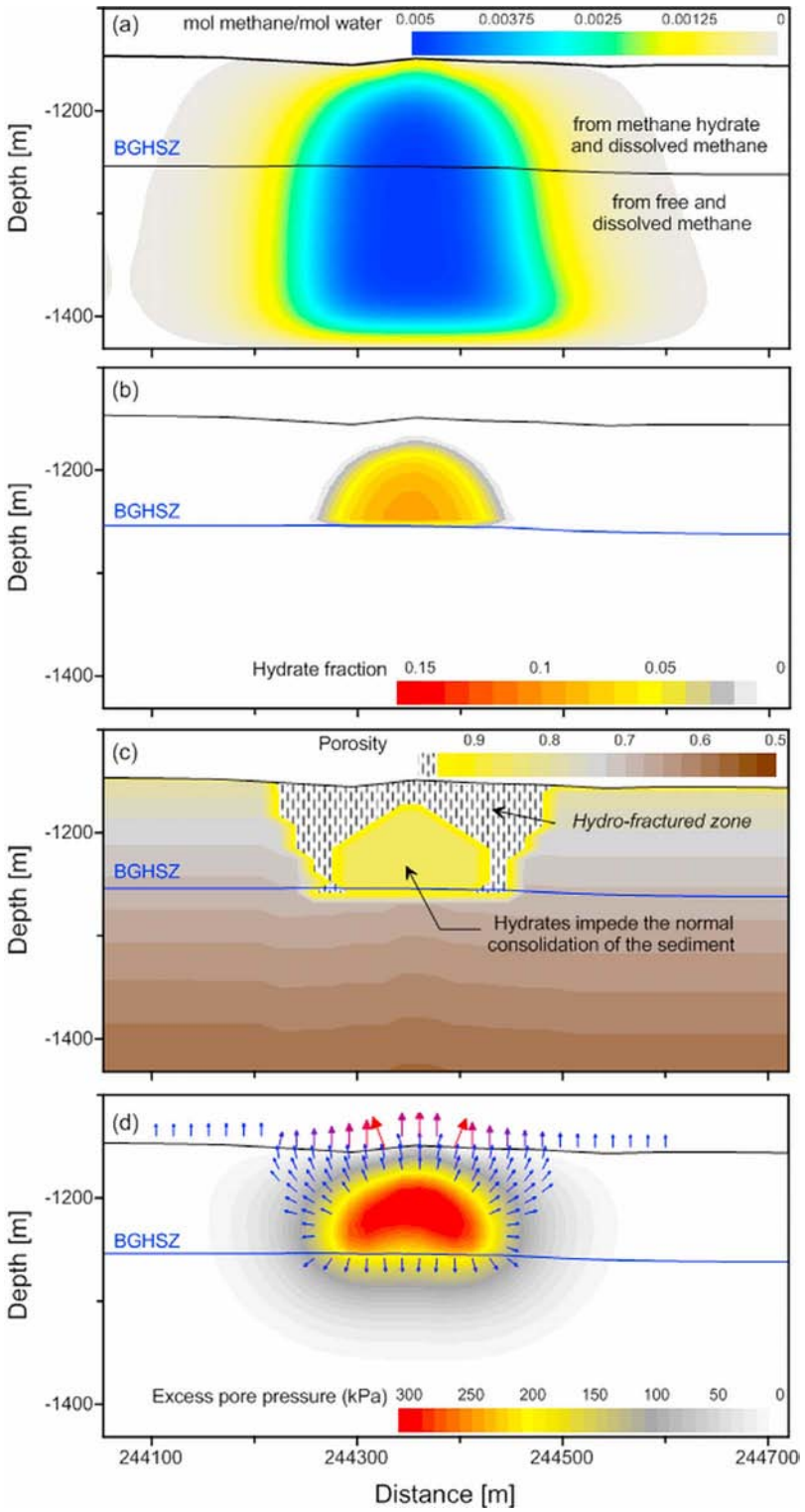

Figure 25. Modeling of the dynamic of the gas hydrate and the dissolution process related to the decrease of the methane concentration at the base of calculation domain. Iso-contours of (a) the methane concentration, (b) the gas-hydrate fraction, (c) the porosity, and (d) the excess pore pressure (contours, measured in kilopascals) at calculation time step of 4000 years. The fluid flow (vector field) is projected on the lower diagram.

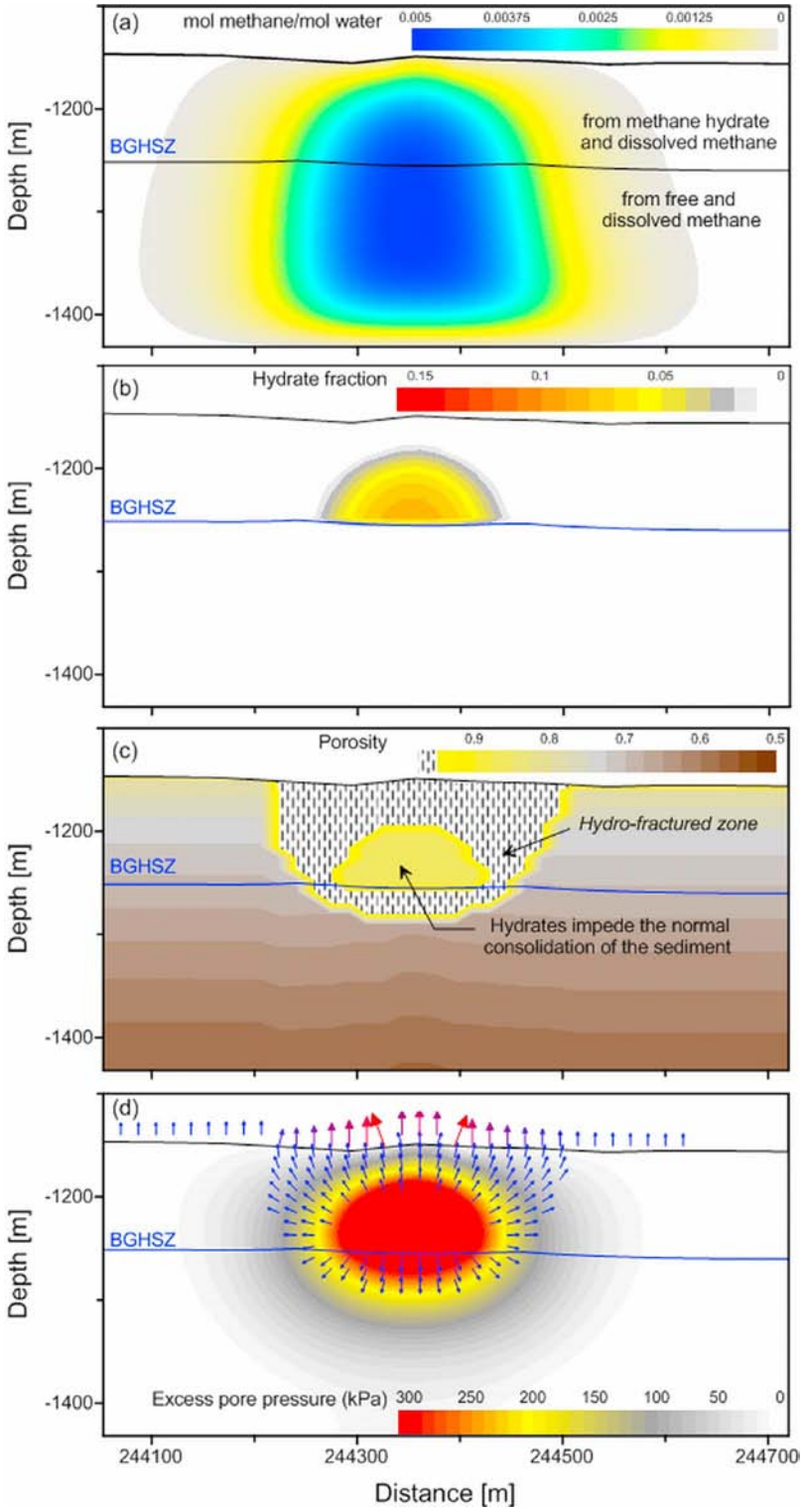

Figure 26. Modeling of the dynamic of the gas hydrate and the dissolution process related to the decrease of the methane concentration at the base of calculation domain. Iso-contours of (a) the methane concentration, (b) the gas-hydrate fraction, (c) the porosity, and (d) the excess pore pressure (contours) at calculation time step of 8000 years. The fluid flow (vector field) is projected on the lower diagram.

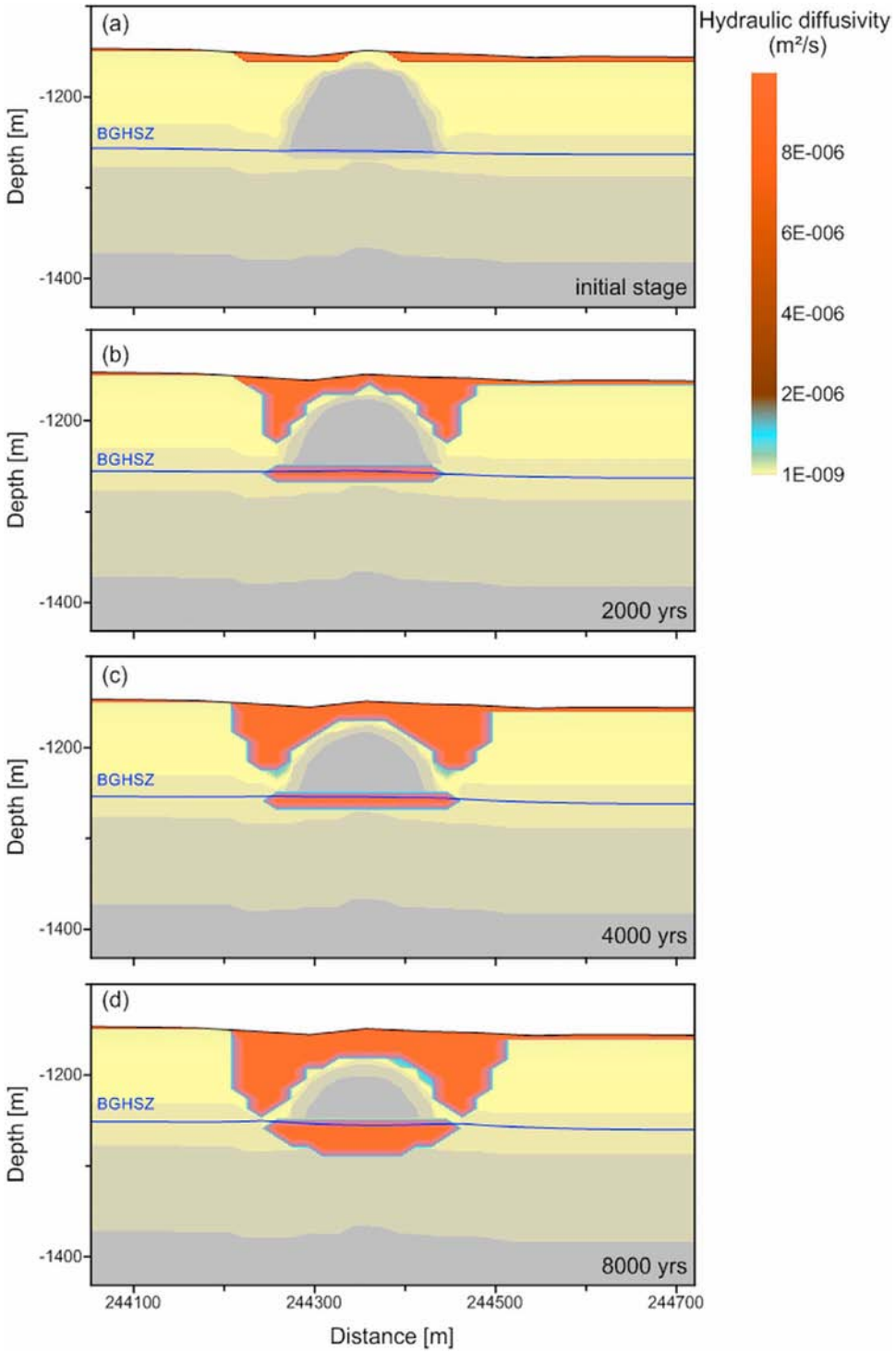

Figure 27. Iso-diffusivity contours used in the calculation and derived from the porosity contours and the hydraulic diffusivities of the hydrate phase and the sediment at (a) 0 yr, (b) 2000 yr, (c) 4000 yr, and (d) 8000 yr. The evolution with time of fractured zones which are characterized by relatively high hydraulic diffusivity shows that the first fractures zones are localized on the periphery of the pockmark.

hydrate dissolution). That is why the simulation presented in Figure 24 to Figure 26 must be considered only qualitatively and as a scheme of the pockmark formation by gas-hydrate dissolution. In order to illustrate the susceptibility of the calculation results to some of the model parameters, four additional case studies were considered by varying only one parameter with respect to the reference calculation (Figure 22 to Figure 27):

[68] - In case 1 the initial methane concentration was taken 30% lower than the one presented in Figure 23.

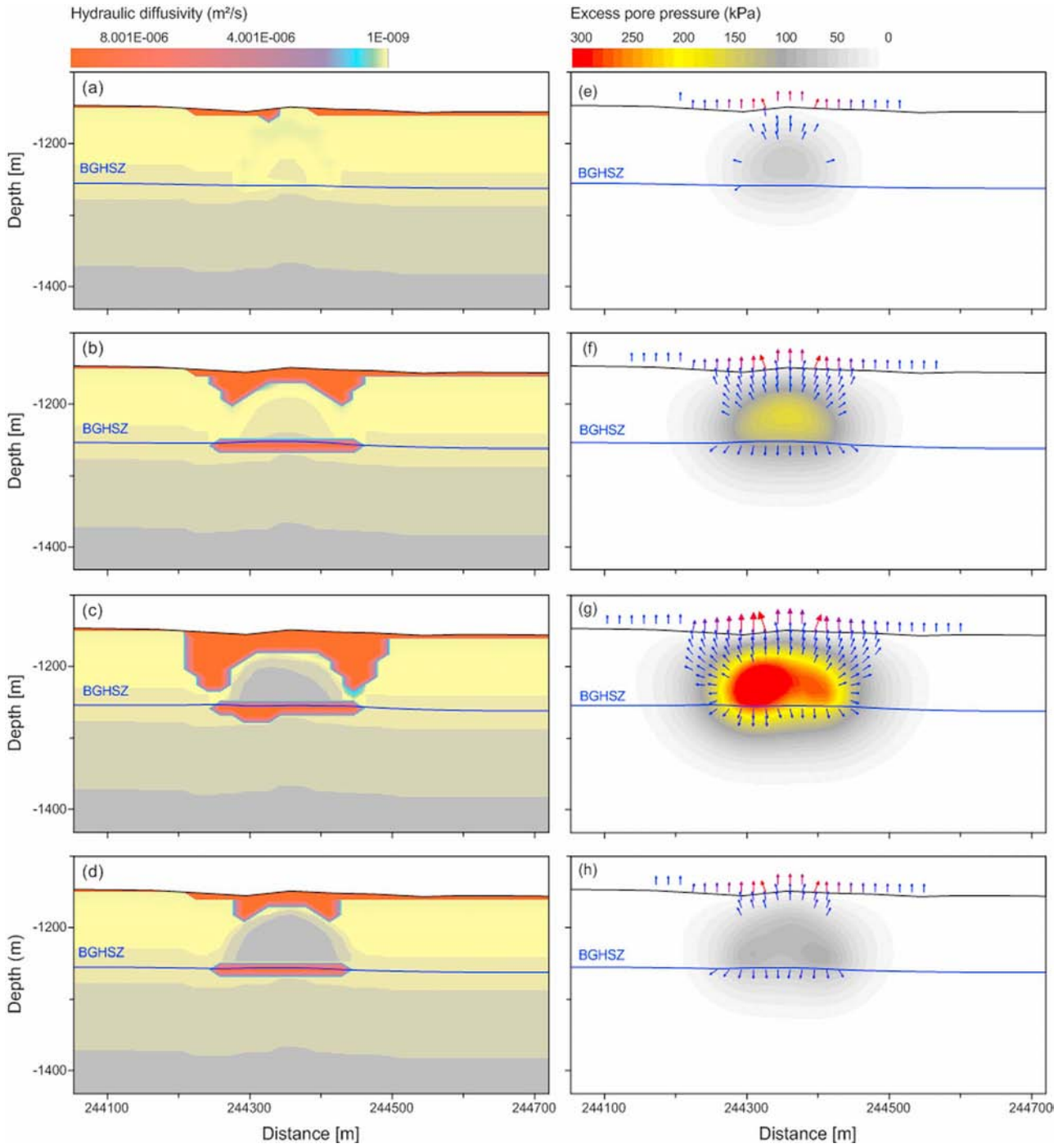

Figure 28. Iso-diffusivity and iso-excess pore pressure contours at calculation step of 4000 years for four different case studies: (a and e) case 1 with an initial hydrate fraction lower than the reference one presented in Figure 23, (b and f) case 2 with a hydraulic diffusivity of the hydrate phase higher than the one used in Figure 23, (c and g) case 3 with a heterogeneous initial hydrate fraction distribution, and (d and h) case 4 with a β (Figure 4) value equal to 20 instead of the β value of 50 used in the reference calculation.

[69] - Case 2 considers a permeability of the pure hydrate one order of magnitude higher than the one used in the reference calculation.

[70] - Case 3 includes a heterogeneous distribution of the gas hydrate with respect to the reference calculation (Figure 23).

[71] - In case 4 the compression index of the hydrated sediment was considered for a β coefficient equal to 20 (for the reference calculation the β was taken equal to 50).

[72] Figure 28 shows the iso-diffusivity and iso-excess pore pressure contours at calculation step of 4000 years for the four different case studies. For case 1 (Figure 28a and

28e), the initial low hydrate fraction generates a very limited amount of excess pore pressure and a localized fractured area at the upper border of the GHOZ. For case 2, the relative high hydraulic diffusivity of the hydrate phase generates a lower amount of excess pore pressure with respect to the reference calculation with a fractured sediments localized in the upper border of the *GHOZ* (Figure 28b and 28f). Case 3 shows a heterogeneous distribution of the pore pressure in the hydrated sediment and therefore generates a heterogeneous distribution of the fractured sediments surrounding the GHOZ. Finally, the low β value leads to a lower amount of excess pore pressure and therefore to a limited fractured zone at the upper boundary of the GHOZ.

[73] For the four case studies, it is clear that the first area were the sediment is expected to fail is localized at the upper boundary of the GHOZ and is similar to the ring shape surrounding the studied pockmarks (Figure 1) confirming that the hydrate dissolution process is the most potential mechanism at the origin of the observed morphology. However, any accurate calculation of the time scale of the pockmark formation and evolution needs an accurate determination of the gas-hydrate distribution in the studied pockmark. This can be only done by calibrating the available VHR seismic data by drilling through the gas-hydrate occurrence zone and recovering sealed hydrates.

6. Conclusions

[74] To the authors' knowledge, this work is the first one to show pockmarks at different stages of maturation based on seafloor and sub-seafloor geophysical data in a relatively localized zone. The interval velocity field combined with piezocone measurements, coring, and SBP profiles show a common internal architecture of the studied pockmarks associated to gas-hydrate dynamics: sediments rich in gas hydrate at the central part of the pockmark surrounded by overpressured sediments. The temperature, pressure, and salinity conditions of the studied area demonstrate that sediment deformation linked to the gas-hydrate dynamics occurs in the hydrate stability zone. Moreover and based on 3-D seismic data and the pseudo-3-D microseismic cube, the sediment deformations (ring shape; Figure 2a) surrounding the central part of the pockmark seem to be localized in the upper sedimentary layers and are not a direct consequence of deep depressions (Figure 19). Modeling results show that the dynamic of the gas flow through faults is the main cause of the hydrate dissolution and as *Rehder et al.* [2004] observed the long-term survival of gas hydrate must be sustained by sufficient supply of gas. The formation of a ring depression around a GHOZ as the one observed in Figure 2 was reproduced theoretically according to the following phases: A decrease of the methane concentration through faults induces the dissolution of the hydrate at the boundary of the sediment-hosted gas hydrate. Hydrate dissolution generates excess pore pressure due to the compaction of the hydrated sediments. The fluid flow generated by the excess pore pressure gets around the gas-hydrate-bearing sediment because of the low permeability of the medium. The loss of the massive hydrate by dissolution at the boundary of the GHOZ and the pore pressure dissipation are accompanied by a sediment fracturing surrounding the sediment hosted gas hydrates.

[75] The simulation of the mechanism of hydrate dissolution can account for an important part of the observed geophysical and geotechnical features. The time scale of the pockmark evolution process remains unknown due to the lack of several key elements and mainly the accurate 3- gas-hydrate distribution in the area. However, we believe that this new research shows how hydrate dissolution in the GHOZ can generate sediment deformation and seafloor collapse.

[76] **Acknowledgments.** We thank J.-C. Caprais and P. Pignet for their help with the salinity measurements. We also thank J.-P. Foucher for helpful discussions. Constructive comments by the associate editor and two anonymous referees greatly helped to improve the paper.

References

Alfaro, M. C., and R. C. K. Wong (2001), Laboratory studies on fracturing of low-permeability soils, *Can. Geotech. J.*, *38*(2), 303–315.

Andersen, K. H., T. Lunne, T. J. Kvalstad, and C. F. Forsberg (2008), Deep water geotechnical engineering, Proc. XXIV National Conference of the Mexican Society of Soil Mechanics, Aguascalientes, 1–57.

Arnaud, J., D. Rappin, J-P. Dunand, and V. Curinier (2004), High-density picking for accurate velocity and anisotropy determination, Proc. 74th Annual International Meeting of the Society of Exploration Geophysicists, Session RC P2.3, 1627–1629.

Badr, O., S. D. Probert, and P. W. Ocallaghan (1991), Atmospheric methane: Its contribution to global warming, *Appl. Energy*, *40*(4), 273–313.

Bigalke, N. K., G. Rehder, and G. Gust (2009), Methane hydrate dissolution rates in undersaturated seawater under controlled hydrodynamic forcing, *Mar. Chem.*, *115*(3–4), 226–234.

Brooks, J. M., W. R. Bryant, B. B. Bernard, and N. R. Cameron (2000), The nature of gas hydrates on the Nigerian continental slope, in *Gas Hydrates: Challenges for the Future*, edited by G. D. Holder and P. R. Bishnoi, vol. 912, pp. 76–93, New York Academy of Sciences, New York.

Burns, S. E., and P. W. Mayne (1998), Monotonic and dilatory pore-pressure decay during piezocone tests in clay, *Can. Geotech. J.*, *35*(6), 1063–1073.

Caprais, J. C., and P. Pignet (2009), Mesures de sulfates et chlorures par chromatographie ionique - campagne ERIG 3D, *Ifremer report 2009/DEEP/LEP/LMEE 09-37*, 23 pages.

Carpenter, G. (1981), Coincident sediment slump/clathrate complexes on the U.S. Atlantic continental slope, *Geo-Mar. Lett.*, *1*, 29–32.

Clennell, B. M., M. Hovland, J. S. Booth, P. Henry, and W. J. Winters (1999), Formation of natural gas hydrates in marine sediments: 1. Conceptual model of gas hydrate growth conditioned by host sediment properties, *J. Geophys. Res.*, *104*(B10), 22,985–23,003.

Cohen, H. A., and K. McClay (1996), Sedimentation and shale tectonics of the northwestern Niger delta front, *Mar. Pet. Geol.*, *13*(3), 313–328.

Corredor, F., J. H. Shaw, and F. Bilotti (2005), Structural styles in the deep-water fold and thrust belts of the Niger delta, *AAPG Bull.*, *89*(6), 753–780.

Damuth, J. E., (1994), Neogene gravity tectonics and depositional processes on the deep Niger delta continental margin, *Mar. Pet. Geol.*, *11*(3), 320–346.

Davie, M. K., and B. A. Buffett (2001), A numerical model for the formation of gas hydrate below the seafloor, *J. Geophys. Res.*, *106*(B1), 497–514.

Davie, M. K., O. Y. Zatsepina, and B. A. Buffett (2004), Methane solubility in marine hydrate environments, *Mar. Geol.*, *203*(1–2), 177–184.

Davis, E. E., G. C. Horel, R. D. Macdonald, H. Villinger, R. H. Bennett, and H. Li (1991), Pore pressures and permeabilities measured in marine-sediments with a tethered probe, *J Geophys. Res.*, *96*(B4), 5975–5984.

Deptuck, M. E., R. A. MacRae, J. W. Shimeld, G. L. Williams, and R. A. Fensome (2003), Revised Upper Cretaceous and lower Paleogene lithostratigraphy and depositional history of the Jeanne d'Arc Basin, offshore Newfoundland, Canada, *AAPG Bull.*, *87*(9), 1459–1483.

Dimitrov, L., and J. Woodside (2003), Deep sea pockmark environments in the eastern Mediterranean, *Mar. Geol.*, *195*(1–4), 263–276.

Durham, W. B., S. H. Kirby, L. A. Stern, and W. Zhang (2003), The strength and rheology of methane clathrate hydrate, *J. Geophys. Res.*, *108*(B4), 2182, doi:10.1029/2002JB001872.

Egorov, A. V., K. Crane, P. R. Vogt, A. N. Rozhov, and P. P. Shirshov (1999), Gas hydrates that outcrop on the sea floor: Stability models, *Geo Mar. Lett.*, *19*, 68–75.

Fang, W. W., M. G. Langseth, and P. J. Schultheiss (1993), Analysis and application of in situ pore pressure measurements in marine-sediments, *J. Geophys. Res.*, *98*(B5), 7921–7938.

Flemings, P. B., H. Long, B. Dugan, J. Germaine, C. M. John, J. H. Behrmann, D. Sawyer, and I. E. Scientists (2008), Pore pressure penetrometers document high overpressure near the seafloor where multiple submarine landslides have occurred on the continental slope, offshore Louisiana, Gulf of Mexico, *Earth Planet. Sci. Lett.*, *274*(1–2), 269–283.

Foland, S. S., N. Maher, and J. W. Yun (1999), Pockmarks along the Californian continental margin: Implications for fluid flow, *AAPG Bull.*, *83*, 681–706.

Foucher, J. P., G. K. Westbrook, A. Boetius, S. Ceramicola, S. Dupre, J. Mascle, J. Mienert, O. Pfannkuche, C. Pierre, and D. Praeg (2009), Structure and drivers of cold seep ecosystems, *Oceanography*, *22*(1), 92–109.

Gay, A., M. Lopez, P. Cochonat, M. Seranne, D. Levache, and G. Sermondadaz (2006), Isolated seafloor pockmarks linked to BSRs, fluid chimneys, polygonal faults and stacked Oligocene-Miocene turbiditic palaeochannels in the Lower Congo Basin, *Mar. Geol.*, *226*(1–2), 25–40.

Georges, R. A., and E. Cauquil (2007), AUV Ultrahigh-Resolution 3D Seismic Technique for Detailed Subsurface Investigations, Offshore Technology Conference, Houston, OTC18784.

Handa, Y. P. (1990), Effect of hydrostatic-pressure and salinity on the stability of gas hydrates, *J. Phys. Chem.*, *94*(6), 2652–2657.

Haskell, N., S. Nissen, D. Whitman, and L. Antrim (1997), Structural features on the West African continental slope delineated by 3-D seismic coherency, *AAPG Bull.*, *81*, 1382.

Haskell, N., S. Nissen, M. Hughes, J. Grindhaug, S. Dhanani, R. Heath, J. Kantorowicz, L. Antrim, M. Cubanski, R. Nataraj, M. Schilly, and S. Wigger (1999) Delineation of geologic drilling hazards using 3-D seismic attributes, *The Leading Edge*, *18*(3), 373–382.

Henninges, J., E. Huenges, and H. Burkhardt (2005), In situ thermal conductivity of gas-hydrate-bearing sediments of the Mallik 5L-38 well, *J. Geophys. Res.*, *110*, B11206, doi:10.1029/2005JB003734.

Heggland, R. (2003), Vertical hydrocarbon migration at the Nigerian continental slope: Applications of seismic mapping techniques, *AAPG Annual Convention*, Salt Lake City, May 11–14, abstr.

Henry, P., M. Thomas, and M. Ben Clennell (1999), Formation of natural gas hydrates in marine sediments: 2. Thermodynamic calculations of stability conditions in porous sediments, *J. Geophys. Res.*, *104*(B10), 23,005–23,022.

Hovland, M., J. W. Gallagher, M. B. Clennell, and K. Lekvam (1997), Gas hydrate and free gas volumes in marine sediments: Example from the Niger delta front, *Mar. Pet. Geol.*, *14*(3), 245–255.

Hovland, M., J. V. Gardner, and A. G. Judd (2002), The significance of pockmarks to understanding fluid flow processes and geohazards, *Geofluids*, *2*(2), 127–136.

Hovland, M., H. Svensen, C. F. Forsberg, H. Johansen, C. Fichler, J. H. Fossa, R. Jonsson, and H. Rueslatten (2005), Complex pockmarks with carbonate-ridges off mid-Norway: Products of sediment degassing, *Mar. Geol.*, *218*(1–4), 191–206.

Hustoft, S., J. Mienert, S. Bunz, and H. Nouze (2007), High-resolution 3D-seismic data indicate focussed fluid migration pathways above polygonal fault systems of the mid-Norwegian margin, *Mar. Geol.*, *245*(1–4), 89–106.

Judd, A. G., and M. Hovland (2007), *Submarine Fluid Flow, the Impact on Geology, Biology and the Marine Environment*, 475 pp., Cambridge Univ. Press, Cambridge, U. K.

Kayen, R. E., and H. G. Lee (1991), Pleistocene slope instability of gas hydrate-laden sediment on the Beaufort Sea margin, *Mar. Geotech.*, *10*, 125–141.

Ker, S., Y. Le Gall, T. Marsset, and P. Leon (2008), SYSIF, a low frequency seismic profiler for near-bottom marine geophysics, 70th EAGE Conference & Exhibition, Rome.

Klauda, J. B., and S. I. Sandler (2003), Predictions of gas hydrate phase equilibria and amounts in natural sediment porous media, *Mar. Pet. Geol.*, *20*(5), 459–470.

Kleinberg, R. L., C. Flaum, D. D. Griffin, P. G. Brewer, G. E. Malby, E. T. Peltzer, and J. P. Yesinowski (2003), Deep sea NMR: Methane hydrate growth habit in porous media and its relationship to hydraulic permeability, deposit accumulation, and submarine slope stability, *J. Geophys. Res.*, *108*(B10), 2508, doi:10.1029/2003JB002389.

Kvenvolden, K. A., and G. D. Redden (1980), Hydrocarbon gas in sediment from the shelf, slope, and basin of the Bering sea, *Geochim. Cosmochim. Acta*, *44*(8), 1145–1150.

Kwon, T. H., G. C. Cho, and J. C. Santamarina (2008), Gas hydrate dissociation in sediments: Pressure-temperature evolution, *Geochem. Geophys. Geosyst.*, *9*, Q03019, doi:10.1029/2007GC001920.

Lee, J. Y., J. C. Santamarina, and C. Ruppel (2010), Volume change associated with formation and dissociation of hydrate in sediment, *Geochem. Geophys. Geosyst.*, *11*, Q03007, doi:10.1029/2009GC002667.

Liu, X. L., and P. B. Flemings (2006), Passing gas through the hydrate stability zone at southern Hydrate Ridge, offshore Oregon, *Earth Planet. Sci. Lett.*, *241*(1–2), 211–226.

Marsset, T., B. Marsset, S. Ker, Y. Thomas, and Y. Le Gall (2010), High and very high resolution deep-towed seismic system: Performance and examples from deep water Geohazard studies, *Deep-Sea Res. Part I*, *57*(4), 628–637, doi:10.1016/j.dsr.2010.01.001.

Masood, T., and J. K. Mitchell (1993), Estimation of in-situ lateral stresses in soils by cone-penetration test, *J. Geotech. Eng.*, *119*(10), 1624–1639.

Masui, A., K. Miyazaki, H. Haneda, Y. Ogata, and K. Aoki (2008), Mechanical Characteristics of Natural and Artificial Gas Hydrate Bearing Sediments, 6th International Conference on Gas Hydrates, edited by P. Englezos and J. Ripmeeser, Vancouver, Canada, July 6–10, 2008, Paper 5697, 8 p.

McIver, R. D. (1982), Role of naturally occurring gas hydrates in sediment transport, *AAPG Bull.*, *66*(6), 789–792.

Masuda, Y., S. Naganawa, S. Ando, and K. Sato, (1997), Numerical calculation of gas production performance from reservoirs containing natural gas hydrates, *SPE* 382901.

Mitchell, J. K., and W. S. Gardner (1975), In situ measurement of volume change characteristics. Proceedings of the ASCE specialty conference on in situ measurements of soil properties, Raleigh, North Carolina, *2*, 279–345.

Moridis, G. J., and K. Pruess (1998), T2SOLV: An enhanced package of solvers for the TOUGH2 family of reservoir simulation codes, *Geothermics*, *27*(4), 415–444.

Ohmura, R., W. Shimada, T. Uchida, Y. H. Mori, S. Takeya, J. Nagao, H. Minagawa, T. Ebinuma, and H. Naritay (2004), Clathrate hydrate crystal growth in liquid water saturated with a hydrate-forming substance: Variations in crystal morphology, *Philos. Mag.*, *84*(1), 1–16.

Pilcher, R., and J. Argent (2007), Mega-pockmarks and linear pockmark trains on the West African continental margin, *Mar. Geol.*, *244*, 15–32.

Rehder, G., S. H. Kirby, W. B. Durham, L. A. Stern, E. T. Peltzer, J. Pinkston, and P. G. Brewer (2004), Dissolution rates of pure methane hydrate and carbon-dioxide hydrate in undersaturated seawater at 1000-m depth, *Geochim. Cosmochim. Acta*, *68*(2), 285–292.

Rempel, A. W., and B. A. Buffett (1997), Formation and accumulation of gas hydrate in porous media, *J. Geophys. Res.*, *102*(B5), 10,151–10,164.

Sahling, H., G. Bohrmann, V. Spiess, J. Bialas, M. Breitzke, M. Ivanov, S. Kasten, S. Krastel, and R. Schneider (2008), Pockmarks in the northern Congo fan area, SW Africa: Complex seafloor features shaped by fluid flow, *Mar. Geol.*, *249*(3–4), 206–225.

Schroeder, C. (1972), Influence of lithology on the mechanical behaviour of rocks in uniaxial compression and Brazilian tests, *Eng. Geol.*, *6*, 31–42.

Sibson, R. H. (2003), Brittle-failure controls on maximum sustainable overpressure in different tectonic regimes, *AAPG Bull.*, *87*(6), 901–908.

Sloan, E. D. (1998), *Clathrate Hydrates of Natural Gases*, Marcel Decker, New York.

Sultan, N. (2007), Comment on "Excess pore pressure resulting from methane hydrate dissociation in marine sediments: A theoretical approach" by Wenyue Xu and Leonid N. Germanovich, *J. Geophys. Res.*, *112*, B02103, doi:10.1029/2006JB004527.

Sultan, N., P. Cochonat, J.-P. Foucher, and J. Mienert (2004), Effect of gas hydrates melting on seafloor slope instability, *Mar. Geol.*, *213*, 379–401.

Sultan, N., M. Voisset, T. Marsset, A. M. Vernant, E. Cauquil, J. L. Colliat, and V. Curinier (2007), Detection of free gas and gas hydrate based on 3D seismic data and cone penetration testing: An example from the Nigerian Continental Slope, *Mar. Geol.*, *240*(1–4), 235–255.

Sultan, N., A. Cattaneo, J. C. Sibuet, J.-L. Schneider, et al. (2009), Deep sea in situ excess pore pressure and sediment deformation off NW Sumatra and its relation with the December 26, 2004 Great Sumatra-Andaman Earthquake, *Int. J. Earth Sci.*, *98*(4), 823–837, doi: 10.1007/s00531-008-0334-z.

Tohidi, B., B. Clennell, R. Anderson, and J. Yang (2004), Gas hydrates studies using high pressure glass micromodels, *AAPG Bull.*, Abstr., *88*(13).

Van der Waals, J. A., and J. C. Platteeuw (1959), Clathrate Solutions, *Adv. Chem. Phys.*, *2*, 2–57.

Waite, W. F., J. C. Santamarina, D. Cortes, B. Dugan, D. N. Espinoza, J. Germaine, J. Jang, J. Jung, T. Kneafsey, H. S. Shin, K. Soga, W. Winters, and T.-S. Yun (2010), Physical properties of hydrate-bearing sediments, *Rev. Geophys.*, *47*, RG4003, doi:10.1029/2008RG000279.

Winters, W. J., I. A. Pecher, W. F. Waite, and D. H. Mason (2004), Physical properties and rock physics models of sediment containing natural and laboratory-formed methane gas hydrate, *Am. Mineral.*, *89*(8–9), 1221–1227.

Xu, W. Y., and L. N. Germanovich (2007), Reply to comment by Nabil Sultan on "Excess pore pressure resulting from methane hydrate dissociation in marine sediments: A theoretical approach", *J. Geophys. Res.*, *112*, B02104, doi:10.1029/2006JB004722.

Xu, W. Y., and C. Ruppel (1999), Predicting the occurrence, distribution, and evolution of methane gas hydrate in porous marine sediments, *J. Geophys. Res.*, *104*(B3), 5081–5095.

Yun, T. S., J. C. Santamarina, and C. Ruppel (2007), Mechanical properties of sand, silt, and clay containing tetrahydrofuran hydrate, *J. Geophys. Res.*, *112*, B04106, doi:10.1029/2006JB004484.

Zatsepina, O. Y., and B. A. Buffett (1997), Phase equilibrium of gas hydrate: Implications for the formation of hydrate in the deep sea floor, *Geophys. Res. Lett.*, *24*(13), 1567–1570.

Zatsepina, O. Y., and B. A. Buffett (1998), Thermodynamic conditions for the stability of gas hydrate in the seafloor, *J. Geophys. Res.*, *103*(B10), 24,127–24,139.

Zhang, Q., G. J. Chen, Q. Huang, C. Y. Sun, X. Q. Guo, and Q. L. Ma (2005), Hydrate formation conditions of a hydrogen plus methane gas mixture in tetrahydrofuran plus water, *J. Chem. Eng. Data*, *50*(1), 234–236.

G. Bayon, B. Marsset, S. Ker, T. Marsset, N. Sultan, and N. Voisset, Ifremer, Département Géosciences Marines, PO Box 70, Plouzané F-29280, France. (nabil.sultan@ifremer.fr)

J. Adamy, E. Cauquil, J. L. Colliat, and D. Drapeau, Total, 92069 Paris La Défense Cedex France.

A. M. Vernant, Cathie Associates, J.E. Mommaertslaan 22, Park Hill, 1831 Diegem, Belgium. (Antoine-Mathieu.Vernant@cathie-associates.com)